

**Modeling tabular icebergs submerged in coupled-to an ocean model**

**A. A. Stern<sup>1</sup>, A. Adcroft<sup>1</sup>, O. Sergienko<sup>1</sup>, G. Marques<sup>1</sup>**

<sup>1</sup>Geophysical Fluid Dynamics Laboratory, Princeton University  
<sup>1</sup>201 Forrestal Rd, Princeton, NJ 08540, USA

**Key Points:**

- A novel modeling framework is developed to explicitly model large tabular icebergs submerged in the ocean.
- Tabular icebergs are represented using Lagrangian elements that drift in the ocean, and are held together by numerical bonds.
- Breaking the numerical bonds allows us to model iceberg breakup and calving.

12 **Abstract**

13 Large tabular icebergs calved from Antarctic ice shelves have long lifetimes (due to their  
 14 large size), during which they drift across large distances, altering ambient ocean circu-  
 15 lation, bottom-water formation, sea-ice formation, and biological primary productivity  
 16 in the icebergs' vicinity. However, despite their importance, the current generation of  
 17 ocean circulation models **usually** do not represent large tabular icebergs. In this study  
 18 we develop a novel framework to model large tabular icebergs submerged in the ocean.  
 19 In this framework, tabular icebergs are represented by **non-levitating** Lagrangian elements  
 20 that **drift are submerged** in the ocean, and . The elements are held together and inter-  
 21 act with each other via bonds. A break of these bonds allows the model to emulate calv-  
 22 ing events (i.e. detachment of a tabular iceberg from an ice shelf) and tabular icebergs  
 23 breaking up into smaller pieces. Idealized simulations of a calving tabular iceberg, its  
 24 drift, and its breakup, demonstrate capabilities of the developed framework.

25 **1 Introduction**

26 Large tabular icebergs - pieces of floating ice with horizontal dimensions substan-  
 27 tially larger than the vertical dimension - calve infrequently ( $\sim$  every forty-fifty years)  
 28 from Antarctic or Greenlandic ice shelves [Jacobs et al, 1992]. Observational estimates  
 29 suggest that over the past 30 years approximately half of Antarctic ice-shelf decay is due  
 30 to iceberg calving, while the other half occurs through ice-shelf melting [Depoorter et  
 31 al, 2013; Rignot et al, 2013]. The infrequently-calved tabular icebergs (horizontal extent  
 32 larger than 5 km) account for more than 90% of the Southern Hemisphere iceberg mass  
 33 [Tournadre et al, 2016].

34 After calving, icebergs drift away from their origins, often becoming stuck in sea  
 35 ice, or grounding on bathymetric highs along the Antarctic coast [Lichy and Hellmer,  
 36 2001; Dowdeswell and Bamber, 2007]. Large tabular icebergs extend deep into the wa-  
 37 ter column, and have the potential to disrupt ocean circulation patterns for months or  
 38 even years after calving [Robinson et al, 2012; Stern et al, 2015]. The freshwater flux from  
 39 iceberg melt impacts ocean hydrography around the iceberg, influencing sea-ice produc-  
 40 tion and bottom-water formation [Arrigo et al, 2002; Robinson et al, 2012; Nicholls et  
 41 al, 2009; Fogwill et al, 2016]. Because of their large size, the tabular icebergs have long  
 42 lifetimes during which they drift over long distances injecting meltwater along the way  
 43 and impacting the Southern Ocean state (e.g. hydrography, sea ice conditions, etc.) far  
 44 away from their calving origins [Stern et al, 2016; Rackow et al, 2017]. Meltwater injec-  
 45 tion (and the accompanying upwelling) from icebergs can also influence biological pro-  
 46 ductivity by bringing nutrients to the surface ocean or changing sea ice conditions [Ar-  
 47 rigo et al, 2002; Vernet et al, 2012; Biddle et al, 2015]. The increased productivity as-  
 48 sociated with free-floating tabular icebergs has been linked with local increases in ocean  
 49 carbon uptake, potentially large enough to be a significant fraction of the Southern Ocean  
 50 carbon sequestration [Smith et al, 2007].

51 In recent years, there has been an increased interest in iceberg drift and decay. This  
 52 surge of interest has been driven by (i) the need to understand polar freshwater cycles  
 53 in order to create realistic climate change and sea level projections [Silva et al, 2006; Shep-  
 54 herd and Wingham, 2007; Rignot et al, 2013]; and (ii) the increased navigation and ex-  
 55 ploration activities in high-latitude iceberg-filled waters in the Arctic [Pizzolato et al,  
 56 2012; Unger, 2014; Henderson and Loe, 2016]. The increased interest in icebergs has led  
 57 to the development of numerical models of iceberg drift and decay [Mountain, 1980; Bigg  
 58 et al, 1997; Gladstone et al, 2001; Kubat et al, 2005], some of which have been included  
 59 in global General Circulation Models [Martin and Adcroft, 2010; Marsh et al, 2015]. These  
 60 iceberg drift models treat icebergs as **levitating** Lagrangian point particles, which are ad-  
 61 vected by the flow, and melt according to parameterizations for icebergs melt. Since ice-  
 62 bergs are treated as point particles, iceberg drift models are mostly suitable for mod-

eling icebergs smaller than an ocean grid cell. Consequently, these models have mostly been used to represent icebergs smaller than 3.5 km on a global scale [Jongma et al, 2009; Martin and Adcroft, 2010; Marsh et al, 2015].

Point-particle iceberg drift models are less suitable for modeling larger tabular icebergs, where the size and structure of the iceberg may be an important feature in determining their drift and decay [Stern et al, 2016]. They also are not suitable for studying the local effects that icebergs have on the surrounding ocean, or the small scale processes that influence iceberg melt and decay [Wagner et al, 2014; Stern et al, 2015]. For these reasons, tabular icebergs are currently not represented in the iceberg drift models used as components of climate models, despite accounting for the vast majority of the total Southern Hemisphere iceberg mass [Tournadre et al, 2016]. **Levitating point-particle iceberg are also largely incompatible with current models or ice shelves and ice shelf cavities.** Since ice shelf models typical allow the ice shelf to displace the water in the water column, it is unclear how one would calve a piece of ice (with finite extent and mass) away from an ice shelf to become a levitating icebergs without triggering artificial tsunamis that would cause the model to crash. **Point-particle iceberg models also do not have any representation of iceberg breakup and calving, which is known to be an important iceberg decay mechanism that influences iceberg trajectories.**

Some efforts have been made to represent tabular icebergs using levitating point particles and to account for the physical presence of the tabular iceberg by introducing additional parametrizations. [Lichy and Hellmer, 2001; Hunke, 2011; Rackow et al, 2017] A promising approach involves integrating ocean properties over the implied iceberg surface area [Rackow et al, 2017] or implied iceberg depth [Hunke, 2011; Merino et al, 2016] (when calculating the iceberg forcing) to account for the horizontal and vertical iceberg extent. This approach could be extended to apply iceberg melt fluxes over a surface area and depth consistent with the implied iceberg shape. However, this approach still does not account for influence that a submerged iceberg can have on the surrounding ocean due to its physical presence in the water column. Martin and Adcroft [2010] attempt to account for the effects of icebergs being submerged in the ocean by allowing their icebergs to apply a pressure to top-most layer of their layered ocean model. This approach effectively allowed the iceberg to displace the ocean, therefore making the point-particle icebergs non-levitating. However, a limitation of this approach is that it the maximum iceberg size was constrained to be smaller than one ocean grid cell, which meant that tabular icebergs could not be represented [Stern et al, 2016].

The goal of this study is to develop a new framework to model all kinds of icebergs, where tabular icebergs are explicitly resolved in the ocean. Our new representation of icebergs aims to include the following key properties: (i) icebergs should be able to travel large distances within the ocean, (ii) icebergs should melt and decay as they drift in the ocean, (iii) icebergs should behave as if they have finite extent **and have arbitrary shape and size** (in order to study local effects that icebergs have on the surrounding ocean), (iv) icebergs should be submerged in the ocean so they are not longer levitating, and (iv) tabular icebergs should be able to break away from ice shelves or break into smaller pieces. Properties (i) and (ii) are common to point-particle icebergs models, while properties (iii) **iv and v and (iv)** are new to the framework developed in this study. A further requirement of the new framework is that the model should run sufficiently **quickly fast** to be used in general circulation models used for climate.

In order to allow icebergs to travel large distances, we model the icebergs in a Lagrangian framework (as in the point particle iceberg drift models described above). However in our model icebergs are no longer treated as point particles that interact with the ocean at a single location. Instead icebergs are given physical structure, so that they interact with the ocean across multiple ocean grid cells, depress the ocean surface over a wide area, and can interact with other icebergs (Figure 1). This is done by assigning a finite surface area and shape to the Lagrangian elements, which allows the elements to

116 behave as if they have a finite extent. The finite extent of an element is transmitted by  
 117 the ocean by distributing the element's weight, surface area and melt fluxes over mul-  
 118 tiple ocean grid cells in a way which is consistent with the shape of the ice element. Finite-  
 119 extent elements interact with each other via repulsive forces which are applied when the  
 120 boundaries of the elements overlap. This prevents the icebergs from piling up on top of  
 121 one another, which has been an issue near coastlines in previous point-particle icebergs  
 122 models.

123 Large tabular icebergs can then be represented by ‘bonding’ together multiple ice  
 124 elements into larger structures using numerical bonds (Figure 1). The numerical bonds  
 125 hold the ice elements together and allow a collection of elements to move as a unit. This  
 126 allows tabular icebergs to drift in the ocean when forced by ocean currents and wind.  
 127 An advantage of representing tabular icebergs using numerical bonds is that by break-  
 128 ing the bonds, we can simulate iceberg calving (e.g.: Figure 2), or the response to an ice-  
 129 berg fracturing into multiple smaller pieces (see movies S1 and S2 in the Supporting In-  
 130 formation).

131 The manuscript is organized as follows. Section 2 gives a description of the key as-  
 132 pects of the model developed in this study. Since this model is a new approach to mod-  
 133 eling icebergs, we present technical aspects of the model. In Sections 3 and 4, we demon-  
 134 strate the capabilities of the model by simulating a tabular iceberg detaching from an  
 135 idealized ice shelf. In a further simulation we break some numerical bonds within the  
 136 tabular iceberg to demonstrate an iceberg splitting in two.

## 137 2 Model description

138 The Kinematic Iceberg Dynamics model (KID) is a Lagrangian particle-based model  
 139 in that the objects of the model are Lagrangian elements. Each element represents a col-  
 140 umn of ice that is floating in the ocean, and has a position, velocity, mass, and a set of  
 141 dimensions, which can evolve in time. The motion of each element is determined by a  
 142 momentum equation which is solved in the (Lagrangian) reference frame of the element.  
 143 The elements experience oceanic and atmospheric forces, which are either prescribed, or  
 144 computed by coupling the iceberg model to an ocean/atmosphere model. The ice ele-  
 145 ments also interact with one another via attractive and repulsive interactive forces, and  
 146 can be bonded together to form larger structures. The angular momentum of the ele-  
 147 ments is not modeled explicitly; instead rotational motion of larger structures emerge  
 148 as a consequence of bond orientation and collective motion.

149 In different contexts, the ice elements can be thought to represent individual ice-  
 150 bergs, sea ice flows, or, when the elements are bonded together, they can represent larger  
 151 structures such as tabular icebergs or ice shelves.

152 The KID model is developed on the code base of an existing iceberg drift model  
 153 [Martin and Adcroft, 2010; Stern et al, 2016]. When run with the correct set of runtime  
 154 flags, the model runs as a traditional point-particle iceberg drift model.

### 155 2.1 Equations of motion

156 The elements drift in the ocean in response to atmosphere, ocean and sea-ice drag  
 157 forces, as well as the Coriolis force, a wave radiation force, a force due to the sea sur-  
 158 face slope and interactive forces with other elements. The momentum equation for each  
 159 element is given by

$$160 M \frac{D\vec{u}}{Dt} = \vec{F}_A + \vec{F}_W + \vec{F}_R + \vec{F}_C + \vec{F}_{SS} + \vec{F}_{SI} + \vec{F}_{IA}, \quad (1)$$

161 where  $\frac{D}{Dt}$  is the total (Lagrangian) derivative,  $M$  is the mass of the element,  $\vec{u}$  is the ve-  
 162 locity of the element, and the terms on the right hand side give the forces on the element

162 due to air drag ( $\vec{F}_A$ ), water drag ( $\vec{F}_W$ ), sea ice drag ( $\vec{F}_{SI}$ ), Coriolis force ( $\vec{F}_C$ ), wave ra-  
163 diation force ( $\vec{F}_R$ ), sea surface slope ( $\vec{F}_{SS}$ ), and interactions with other elements ( $\vec{F}_{IA}$ ).

164 When ice elements move alone (without interactions with other elements), they can  
165 be thought of as representing individual (or clusters of) small icebergs, and follow the  
166 same equations described in the iceberg drift model of Martin and Adcroft [2010] (based  
167 on the equations outlined in Bigg et al [1997] and Gladstone et al [2001]). A description  
168 of these forces is provided for completeness in Appendix A.

169 In addition to the external forces, the ice elements experience interactive forces due  
170 to the presence of other elements. Two types of interactive forces are included between  
171 elements. The first force is a repulsive force which is applied to elements to prevent them  
172 from overlapping the boundaries of the neighboring elements. The second interactive force  
173 is a force due to numerical ‘bonds’, and is only applied if two elements are labelled as  
174 ‘bonded’. When two elements are bonded, each element feels an attractive force that pre-  
175 vents the elements from moving too far apart from one another. The details of the in-  
176 teractive forces are provided in below.

## 177 2.2 Interactive Forces

178 The interactive forces in the model are used to (i) prevent the ice elements from  
179 overlapping and (ii) to connect multiple ice elements together so that the collection of  
180 elements moves as a rigid body. Modeling the collisions and movements of rigid objects  
181 precisely, requires very small time steps and precise collision detection algorithms, which  
182 are very computationally expensive. Models using these methods are typically only run  
183 for a few days or even a few seconds, and are used to study rapid processes like crack  
184 formation or ridging [Hopkins, 2004; Bassis and Jacobs, 2013; Rabatel et al, 2015]. The  
185 tabular iceberg framework presented in this study is developed in order to be used in gen-  
186 eral circulation models used for multi-year simulations. In order to gain the required com-  
187 putational efficiency, we relax the requirement that icebergs must be perfectly rigid and  
188 that ice elements can not overlap. Instead, we model the interactive forces between ice  
189 elements using damped elastic forces, which can be calculated more efficiently.

190 The total interactive force on an element is calculated by adding together the in-  
191 teractions with all other elements, such that the interactive force on element  $i$ ,  $(\vec{F}_{IA})_i$   
192 is given by:

$$(193) \quad (\vec{F}_{IA})_i = \sum_{j \neq i} (\vec{F}_{IA})_{ij}, \quad (2)$$

194 where  $(\vec{F}_{IA})_{ij}$  is the force on element  $i$  by element  $j$ . Both bonded and repulsive inter-  
195 actions are modeled using elastic stresses with frictional damping. The elastic compo-  
196 nent of the force is a function of the distance between the two elements, while the fric-  
197 tional damping force depends on the relative velocity of the two elements.

198 To describe the forces between two elements, we begin by introducing some nota-  
199 tion. Let  $\vec{x}_i$ ,  $\vec{x}_j$  be the positions of elements  $i$  and  $j$ . The distance between elements  $i$   
200 and  $j$  is

$$(201) \quad d_{ij} = |\vec{x}_i - \vec{x}_j|. \quad (3)$$

202 In calculations of the interactive forces between elements, the elements are assumed to  
203 be circular. We define the interaction radius of an element by

$$(204) \quad R_i = \sqrt{\frac{A_i}{\pi}}, \quad (4)$$

205 where  $A_i$  is the planar surface area of element  $i$ . Using this, we define the critical-interactive-  
length scale,

$$(206) \quad L_{ij} = R_i + R_j, \quad (5)$$

207 which governs interactions between elements  $i$  and  $j$ . Repulsive forces are only applied  
208 when  $d_{ij} < L_{ij}$ , while for  $d_{ij} > L_{ij}$  attractive bonded forces are applied when a bond ex-

206 lists between element  $i$  and  $j$  (see diagram in Figure 3). The interactive forces are de-  
 207 signed such that (in the absence of other external forces) bonded particles will settle in  
 208 an equilibrium position where elements are separated by  $L_{ij}$ .

209 To aid in notation, we define a bond matrix  $B_{ij}$  such that  $B_{ij} = 1$  if elements  $i$   
 210 and  $j$  are bonded together and  $B_{ij} = 0$  otherwise. Using this notation, the interactive  
 211 force  $(\vec{F}_{IA})_{ij}$  on an element  $i$  by an element  $j$  is given by

$$(\vec{F}_{IA})_{ij} = \begin{cases} (\vec{F}_e)_{ij} + (\vec{F}_d)_{ij} & \text{if } d_{ij} \leq L_{ij} \\ (\vec{F}_e)_{ij} + (\vec{F}_d)_{ij} & \text{if } d_{ij} > L_{ij} \text{ and } B_{ij} = 1 \\ 0 & \text{if } d_{ij} > L_{ij} \text{ and } B_{ij} = 0. \end{cases} \quad (6)$$

212  $(\vec{F}_e)_{ij}$  and  $(\vec{F}_d)_{ij}$  are the elastic and frictional damping components of the interactive  
 213 force between elements  $i$  and  $j$ . The elastic force  $(\vec{F}_e)_{ij}$  between elements is given by

$$(\vec{F}_e)_{ij} = -\kappa_e \left( d_{ij} - L_{ij} \right) M_{ij} \vec{r}_{ij}, \quad (7)$$

214 where  $\vec{r}_{ij} = \frac{(\vec{x}_i - \vec{x}_j)}{|\vec{x}_i - \vec{x}_j|}$  is the directional unit vector between the position of element  $i$  and  
 215  $j$ ,  $\kappa_e$  is the spring constant, and  $M_{ij}$  is the minimum of the masses of elements  $i$  and  $j$ .  
 216 The interactive forces obey Newton's 3rd Law (i.e.:  $(\vec{F}_{IA})_{ij} = -(\vec{F}_{IA})_{ji}$ ). The mini-  
 217 mum mass,  $M_{ij}$ , is preferred to the average mass, since this means that for two bonded  
 218 elements a fixed distance apart, the acceleration due to elastic forces is bounded, even  
 219 when the mass of one of the elements approaches zero.

220 The frictional damping force acts to dampen the relative motion of the two par-  
 221 ticles. If  $\vec{r}_{ij}^\perp$  is the direction vector perpendicular to  $\vec{r}_{ij}$ , and  $P_{\vec{r}_{ij}}$  and  $P_{\vec{r}_{ij}^\perp}$  are the pro-  
 222 jection matrices that project onto  $\vec{r}_{ij}$  and  $\vec{r}_{ij}^\perp$  respectively, then the frictional damping  
 223 force is given by

$$(\vec{F}_d)_{ij} = M_{ij} \left( -c_{r_{||}} P_{\vec{r}_{ij}} - c_{r_\perp} P_{\vec{r}_{ij}^\perp} \right) \cdot (\vec{u}_i - \vec{u}_j) \quad (8)$$

224 Here  $c_{r_{||}}$  and  $c_{r_\perp}$  are the drag coefficients for the damping motion parallel and perpen-  
 225 dicular to  $r_{ij}$ , respectively. We set  $c_{r_{||}} = 2\sqrt{\kappa_e}$ , so that the elastic force parallel to  $\vec{r}_{ij}$   
 226 is critically damped. The perpendicular drag coefficient is set to  $c_{r_\perp} = \frac{1}{4}c_{r_{||}}$ . The per-  
 227 pendicular damping force is used reduce the relative motion of ice elements passing by  
 228 one another with overlapping boundaries. The damping forces are implemented using  
 229 an implicit time stepping scheme, to avoid stability issues for very small elements (de-  
 230 tails found in Appendix B).

231 Figure 4 illustrates the effectiveness of the repulsive forces in an uncoupled (ice-  
 232 only) simulation. In this simulation ice elements are forced westward into a bay, and even-  
 233 tually come to rest in the bay with a small amount of overlap between elements. The  
 234 amount of overlap between elements in the final state of the simulation depends on the  
 235 magnitude of the spring constant,  $\kappa_e$ , with larger spring constants reducing the amount  
 236 of overlap. Increasing the spring constant also makes the system numerically stiff so that  
 237 smaller time steps are required to prevent numerical instabilities (the system is stable  
 238 for time steps satisfying  $dt^2 < 4/\kappa_e$ ). A value of  $\kappa_e = 10^{-5}$  is chosen that is large enough  
 239 to prevent too much overlap between elements for typical ocean forcings (e.g: Figure 4),  
 240 and small enough to allow for time steps up to 10 minutes (smaller time steps are used  
 241 when the model is coupled to an ocean model).

242 Figure 5 illustrates the effectiveness of the numerical bonds in simulations of small  
 243 icebergs (individual un-bonded elements) and large icebergs (constructed from many ice  
 244 elements bonded together) forced to drift towards a convex coast line. When the tab-  
 245 ular icebergs arrive at the coast, they bump into the coastline and begin to rotate, in-  
 246 fluencing the paths of the other icebergs. This example illustrates an advantage of us-  
 247 ing small elements bonded together to represent large-scale structure - i.e. rotational mo-  
 248 tion of large structures can be simulated without explicitly accounting for the angular

momentum of the elements (as discussed in Jakobsen [2001]). Movies of these uncoupled simulations are found in S3 and S4 in the Supporting Information.

### 2.3 Initializing element geometry and packing

For purposes of initialization, we assume that elements have surface areas which are shaped as equally-sized regular hexagons (note that the elements are assumed to be circular for purposes of interactions). When packing elements together, the hexagonal elements are initially arranged in a staggered lattice, with each element bonded to the adjacent elements (Figures 1 and 6a). In this arrangement, each element (away from the edges) is bonded to six other elements. The bonds between elements form a pattern of equilateral triangles, which gives rigidity to the larger structure. The circular shape of elements (used for interactions) is inscribed within the hexagonal shape used for packing (Figure 6a). The centers of adjacent elements are initially separated by a distance  $d_{ij} = L_{ij} = 2A_p$ , where  $A_p$  is the length the apothems of the hexagons.

Some experiments were also performed using rectangular elements, arranged in a regular (non-staggered) lattice. In this case, each element forms four bonds with adjacent elements. However, the resultant structures were found to be much less rigid and tended to collapse when sufficient forces was applied. For this reason, we only show the results using hexagonal elements.

### 2.4 Ocean-ice and ice-ocean coupling

The KID model is coupled to the ocean model via a two-way synchronous coupling, meaning that ocean-model fields are passed to the iceberg model, and iceberg model fields are passed back to the ocean model at every time step. Passing fields between the two models involves interpolating the fields from the ocean model's Eulerian grid onto the iceberg model's 'Lagrangian grid' (i.e.: onto the ice elements), and aggregating fields from the Lagrangian elements onto the ocean-model's Eulerian grid.

The coupling from the ocean model to the iceberg model is straight forward: at every time step: the ocean mixed layer temperature, salinity, velocity and sea-ice concentration are passed from the ocean model to the iceberg model, to be used in the momentum and thermodynamic equations of the ice elements. Since tabular icebergs are explicitly resolved in the ocean, it is sufficient for each element to interact with ocean mixed layer only (i.e.: there is no need to manually embed icebergs into the ocean by integrating ocean fields over the icebergs' thickness, as suggested in Merino et al [2016]). Within the iceberg model, the ocean model fields are interpolated onto the Lagrangian grid using a bilinear interpolation scheme.

The iceberg model influences the ocean by: (i) applying a pressure to the ocean surface, (ii) affecting the upper ocean by applying a no-slip boundary condition and frictional velocity beneath the ice, and (iii) imposing heat, salt and mass fluxes on the ocean, associated with ice melting. Six fields are passed from the iceberg model to the ocean model: ice mass, ice area, frictional velocity, and heat, salt and mass fluxes. Fields in the iceberg model are aggregated from the Lagrangian elements to the Eulerian ocean grid before they are passed to the ocean model.

The aggregation of the iceberg-model fields onto the ocean grid is done in a way that is consistent with the shape of the elements in the iceberg model (see Section 2.3). Fields are 'spread' to the ocean model grid by exactly calculating what fraction of an element's surface area lies in a particular grid box, and dividing the field in proportion to this fraction. As an example, consider a hexagonal element in the iceberg model, which is positioned such that it intersects four ocean grid cells (Figure 6b). In this situation, the element's mass (for example) is divided between these four ocean cells in proportion to the overlap area between the hexagonal element and the grid cell (this fraction is shown

298 by the colors in Figure 6b). An advantage of this approach is that there are no jumps  
 299 in pressure as an element moves from one grid cell to another, which could trigger ar-  
 300 tificial tsunamis within the ocean model, making the ocean model unrealistic.

301 The numerical calculation of the intersection between hexagons and the ocean grid  
 302 is simplified by dividing the hexagon into 6 equilateral triangles. This method allows for  
 303 the intersection to be found even when the hexagon is not aligned with the grid.

304 The aggregation scheme is coded with the restriction that an element's area can  
 305 only intersect a maximum of four ocean grid cells at a time. A consequence of this is that  
 306 this sets a limit on the maximum size of elements that can be represented using this model,  
 307 i.e.: the longest horizontal dimension of an ice element must be smaller than the ocean  
 308 grid spacing. Larger ice structures are constructed by bonding together smaller elements.

## 309 2.5 Melting parameterization

310 The ice elements change their mass and size due to melting, which also affects the  
 311 surrounding ocean by changing its heat and salt content. In the model, these processes  
 312 are parametrized in several ways. In this section we described the melt parametrization  
 313 for bonded, unbonded and partially bonded elements.

314 As mentioned above, ice elements which do not interact with other elements are  
 315 modeled identically to the point particle icebergs described in Martin and Adcroft [2010].  
 316 These elements melt according to three semi-empirical parametrization for melt com-  
 317 monly used in previous iceberg studies [Gladstone et al, 2001; Martin and Adcroft, 2010].  
 318 Three types of iceberg melting are distinguished: basal melt,  $M_b$ , melt due to wave ero-  
 319 sion,  $M_e$  and melt due to buoyant convection,  $M_v$ .  $M_e$  and  $M_v$  are applied to the sides  
 320 of the ice element, while  $M_b$  is applied at the ice element base. The details of  $M_b$ .  $M_v$   
 321 and  $M_e$  are given in Appendix A.

322 When multiple elements are bonded together to form larger structures, it is no longer  
 323 appropriate to use the melt parameterizations developed for individual point-particle ice-  
 324 bergs. An element which is completely surrounded by other elements, is meant to rep-  
 325 resent a column of ice in the middle of a large structure, and hence will not experience  
 326 melt at its sides due to wave erosion or buoyant convection. Also, the iceberg basal melt  
 327 rate,  $M_b$  described above is based on boundary layer theory of flow past a finite plate,  
 328 and is only appropriate for basal surfaces where the distance from the leading edge is  
 329 sufficiently small [Eckert, 1950; Weeks and Campbell, 1973]. For an element in the in-  
 330 terior of a large structure, the distance from the edge of the structure is large, and so  
 331 using  $M_b$  for the basal melt is not appropriate. Instead, the basal melt,  $M_s$  is determined  
 332 using the three equation model for basal melt, which is a typical melting parametriza-  
 333 tion used beneath ice shelves [Holland and Jenkins, 1999].

334 When using both individual elements and bonded elements in the same simulation,  
 335 we determine which melt rate parameterizations to use based on the amount of bonds  
 336 that each element has. An element in the center of a large structure has the maximum  
 337 number of bonds, while un-bonded elements has no bonds. If an element can have max-  
 338 imum number of bonds  $N_{max}$ , and the number bonds that an element has is  $N_b$ , then  
 339 this element experiences the side melt and bottom melt

$$M_{side} = \frac{(N_{max} - N_b)}{N_{max}} (M_v + M_e) \quad (9)$$

340 and

$$M_{bottom} = \frac{(N_{max} - N_b)}{N_{max}} M_b + \frac{N_b}{N_{max}} M_s \quad (10)$$

341 respectively. In this way, elements with no bonds, melt like point-particle icebergs; el-  
 342 ements at the center of large structures melt like ice shelves; and elements at the sides  
 343 of large structures have a combination of iceberg side and basal melt, and ice-shelf melt.

## 344 2.6 Algorithms and computational efficiency

345 Including interactions between elements leads to an increase in the computational  
 346 complexity of the model. In this subsection we comment on some of the algorithmic pro-  
 347 cedures that have been used to increase the computational efficiency.

### 348 2.6.1 Interactions and Bonds

349 At every time step, we calculate the force on each element due to interactions with  
 350 every other element. This involves order  $N^2$  operations (for N elements), which becomes  
 351 computational expensive as N grows large. We reduce the number of computations by  
 352 leveraging the fact that each element only has repulsive interactions with elements that  
 353 are less than one ocean grid cell away, and each element only has bonded interactions  
 354 with a small number of other elements.

355 The computation reduction is achieved by storing the element data in an efficient  
 356 way that eliminates a search through all element pairs to check if they are close to one  
 357 another or are bonded with one another. The data storage system is organized as fol-  
 358 lows: pointers to the memory structures containing each element are stored in linked list  
 359 data structures, which allow elements to be added and removed from the lists easily with-  
 360 out restructuring the entire list. Instead of using one list for all the elements on a pro-  
 361cessor (as was done in the original code [Martin and Adcroft, 2010]), we use a separate  
 362 linked list for each ocean grid cell. When an element moves between ocean grid cells, it  
 363 is removed from its original list and added to the list corresponding to its new ocean grid  
 364 cell. Since the area of elements has to be smaller than the area of an ocean grid cell, the  
 365 critical interaction length scale (equation 5) is less than the size of a grid cell. This means  
 366 that elements only experience repulsive forces with other elements in the same ocean grid  
 367 cell, or in one of the 8 adjacent cells. At each time step and for each element  $i$ , the code  
 368 traverses the linked lists of the 9 surrounding grid cells, and applies a repulsive force if  
 369  $d_{ij} < L_{ij}$  (whether the elements are bonded or not). Limiting the possible repulsive  
 370 interactions to elements in these 9 linked lists substantially reduces the computational  
 371 time needed to calculate the total interactive forces.

372 The attractive forces are computed in a following way. Each bond is assigned a piece  
 373 of memory. Each ice element contains a linked list of each of its bonds (typically up to  
 374 six bonds per element). At every time step, the code traverses the lists of bonded ele-  
 375 ments, and adds an attractive bonded force corresponding to these bonds if  $d_{ij} > L_{ij}$   
 376 (the repulsive bonded force to be applied when  $d_{ij} < L_{ij}$  is already accounted for by  
 377 the procedure outlined in the previous paragraph). Having a list of bonds stored with  
 378 each element reduces the computations needed for bonded interactions from order  $N^2$   
 379 to order N. Computing attractive forces separately from the repulsive forces allows us  
 380 to avoid checking whether two elements are bonded, which further increases the com-  
 381 putational efficiency.

### 382 2.6.2 Parallelization and halos

383 The iceberg model runs on multiple processors in parallel (using the same grid de-  
 384 composition as the ocean model). When elements move from an ocean cell on one pro-  
 385cessor to an ocean cell on a second processor, the memory has to be passed from one pro-  
 386cessor to the next, added and removed to the appropriate lists and the memory has to be  
 387 allocated and deallocated correctly. Element interactions across the edge of processors  
 388 are handled using computational halos. A computational halo is a copy of the edge of  
 389 a one processor which is appended to the edge of a second processor, so that the first  
 390 processor can interact with the second processor during a time step. Before each time  
 391 step, elements at the edges of each processor are copied onto the halos of adjacent pro-  
 392 cessors so that they can be used in calculating the interactive forces. After each time step,

393 these halos are emptied, and the process is repeated. These halo updates are one of the  
 394 most computationally expensive parts of the iceberg model. Details of how the bonds  
 395 are broken and reconnected across processor boundaries are provided in Appendix C.

### 396 2.6.3 Time stepping

397 The elements in the iceberg model are advected using a semi-implicit velocity Ver-  
 398 let time-stepping scheme. The velocity Verlet time stepping scheme is commonly used  
 399 in discrete element models in video games because it is computational efficient and has  
 400 desirable stability properties [Jakobsen, 2001]. This time stepping scheme was preferred  
 401 to the Runge-Kutta 4, which was used in the iceberg model of Martin and Adcroft [2010]  
 402 since the Verlet time stepping only requires one calculation of the interactive forces once  
 403 per time step (while the Runge-Kutta scheme requires the interactive forces to be cal-  
 404 culated four times). Since the calculation of the interactive forces is one of the most com-  
 405 putationally expensive part of the algorithm, the Verlet scheme leads to a significant in-  
 406 crease in the computational efficiency of the model. The Verlet scheme used in the model  
 407 contains a modification of the original (fully explicit) velocity Verlet time stepping scheme  
 408 in that damping terms are treated implicitly (which increases the numerical stability).  
 409 The details of this adapted time stepping scheme are outlined in Appendix B.

## 410 3 Experiment Setup

411 The introduction of Lagrangian elements, numerical bonds and interpolation schemes  
 412 between the Eulerian and Lagrangian grids (discussed in Section 2) means that we now  
 413 have the tools to model large tabular icebergs submerged in the ocean. We demonstrate  
 414 this capability by simulating a tabular iceberg drifting away from an ice shelf in ideal-  
 415 ized setting.

### 416 3.1 Model configuration

417 We use the geometric setup of the Marine Ice Ocean Modeling Inter-comparison  
 418 Project (MISOMIP) [Asay-Davis et al, 2016]. The configuration consists of an idealized  
 419 ice shelf in a rectangular domain. The domain is  $L_x = 80$  km wide and  $L_y = 480$  km  
 420 long, and contains an ice shelf which is grounded on the south side of the domain and  
 421 has an ice front at  $y=650$  km. The ice thickness and bottom topography of this setup  
 422 are shown in Figure 7a and 7c respectively, with the grounding line position drawn in  
 423 for reference. The configuration is the same as that of the Ocean0 setup in the MISOMIP,  
 424 with a few minor changes to the ice-shelf geometry (see the Supporting Information for  
 425 details).

### 426 3.2 Initializing Lagrangian elements:

427 The idealized ice shelf is constructed out of Lagrangian ice elements. Ice elements  
 428 are hexagonal and are arranged in a regular staggered lattice (as discussed in Section  
 429 2.3). The sides of the hexagons are initialized with length  $S = 0.98$  km. Gaps along  
 430 the boundaries are filled in using smaller elements so that the total ice-shelf area is pre-  
 431 served. The initial mass of the ice elements is determined by a preprocessing inversion  
 432 performed before the model is run. The initial ice thicknesses of the elements are cal-  
 433 culated from the ice mass by assuming that the ice has a constant density,  $\rho$ . The draft  
 434 and freeboard are related to the ice thickness by  $T = F + D$  and  $D = \frac{\rho}{\rho_o}T$ , where  $\rho$   
 435 and  $\rho_o$  are the density of ice and seawater respectively. When the model runs, the mass  
 436 of elements is aggregated from the Lagrangian grid onto the Eulerian ocean grid (see Sec-  
 437 tion 2.3), and is used to find the surface pressure and ice draft (part of an ice column  
 438 submerged into the ocean). The ice draft calculated without the aggregation (treating

elements as point masses) contains large grid artifacts (Figures 7b). These grid artifacts are much reduced after the mass-spreading aggregation is used (Figure 7c).

### 441 3.3 Ocean model setup

442 The KID model is coupled to the MOM6 ocean model [Hallberg et al, 2013]. The  
 443 ocean model configuration uses a vertical coordinate system which is a hybrid between  
 444 a sigma-level and a z-level coordinate. In particular, model layers deform underneath the  
 445 ice shelf as they would in a sigma-coordinate model, but collapse to zero thickness when  
 446 they intersect with bottom topography, as they would in a z-level model. The coordi-  
 447 nate system was achieved using ALE regridding-remapping scheme [White et al, 2009].  
 448 The model uses a horizontal resolution of 2 km, and 72 vertical layers. All simulations  
 449 were repeated using the ocean model configured in isopycnal mode (results were simi-  
 450 lar and are not presented here).

451 Ocean parameters are as specified in the MISOMIP configuration [Asay-Davis et  
 452 al, 2016], and are shown in Table 1. The simulation is initially at rest, with horizontally  
 453 uniform initial ocean temperature and salinity profiles which vary linearly between spec-  
 454 ified surface and bottom values:  $T_{top} = -1.9^\circ \text{C}$ ,  $T_{bottom} = 1.0^\circ \text{C}$ ,  $S_{top} = 33.8 \text{ psu}$ ,  
 455  $S_{bottom} = 34.7 \text{ psu}$ . The maximum ocean depth is  $H_{ocean} = 720 \text{ m}$ . A sponge layer is  
 456 used on the northern boundary of the domain, which relaxes the temperature and salin-  
 457 ity back to the initial temperature and salinity profile. The sponge layer has length  $L_{sponge}$   
 458 = 10 km, and has a relaxation time scale parameter  $T_{sponge} = 0.1 \text{ days}$  at the north-  
 459 ern boundary. The inverse of the relaxation time scale parameter drops linearly to zero  
 460 over the length of the sponge layer. Melting is set to zero for ocean cells where the ocean  
 461 column thickness is less than 10m to avoid using more energy to melt ice than is present  
 462 in the water column.

### 463 3.4 Spinup period:

464 The model is spun-up for 5 years with all ice elements being fixed. During spinup,  
 465 the injection of buoyant meltwater at the base of the ice shelf drives a clockwise circu-  
 466 lation within the domain (not shown). The circulation compares well with an identical  
 467 static ice-shelf experiment run using an Eulerian ice shelf model [Goldberg et al, 2012].  
 468 A detailed comparison of the Lagrangian and Eulerian ice shelf models is presented in  
 469 a separate study, and is not shown here.

### 470 3.5 Iceberg calving:

471 After spinup, a large tabular iceberg detaches from the ice shelf, and is allowed to  
 472 drift into the open ocean. This is achieved by allowing all ice elements initially within  
 473 a 14.4 km radius of the center of the ice front to move freely while the other ice elements  
 474 continue to be held stationary. Ice elements less than 12 km from the center of the ice  
 475 front, are bonded together to form a semi-circular tabular iceberg. A ring of elements  
 476 whose distance,  $d$ , from the ice front center obeys  $12 \text{ km} \leq d \leq 14.4 \text{ km}$ , are allowed  
 477 to move freely, but have all their bonds removed. Elements in this half annulus repre-  
 478 sent fragments of the ice shelf which calve into small pieces during the calving event.

479 After the spinup period, a wind stress  $\vec{\tau} = < \tau_x, \tau_y > = < 0.05, 0.05 > \frac{N}{m^2}$  is ap-  
 480 plied to drive the tabular iceberg away from the ice-shelf cavity. This is referred to as  
 481 the Control simulation. Perturbation experiments were also performed using other wind  
 482 stress values. Further perturbation experiments were performed by breaking some nu-  
 483 merical bonds in order to break the tabular iceberg into smaller pieces.

484 **4 Model Results**

485 After spinup of the Control simulation, the elements near the ice-shelf front are al-  
 486 lowed to move freely, and the icebergs begin to drift away from the ice shelf while fully  
 487 submerged in the ocean (see Figures 2 and 8, and the movie S1 in the Supporting In-  
 488 formation). At this point, the iceberg model and the ocean model are fully coupled: changes  
 489 to the iceberg position alter the top-of-ocean pressure and dynamical boundary condi-  
 490 tion; and changes to the iceberg melt rates alter the top-of-ocean temperature, salt and  
 491 mass fluxes. These changing ocean boundary conditions influence the ocean by trigger-  
 492 ing gravity waves, driving surface mixing, and affecting the ocean stratification. The evolv-  
 493 ing ocean velocities, temperatures and salinities feedback onto the ice elements by chang-  
 494 ing the force balance on the ice elements (leading to changes in the elements' position),  
 495 and altering the melt rates. The various feedbacks within this coupled system offer many  
 496 opportunities for the model to become unstable. The fact that the model is stable and  
 497 that we are able to simulate tabular icebergs moving in the ocean without the model-  
 498 ing crashing and introducing artificial effects like tsunamis, is a non-trivial technical mile-  
 499 stone.

500 **4.1 Iceberg motion**

501 In the Control simulation, the semi-circular tabular iceberg moves as a cohesive unit  
 502 due to the presence of the numerical bonds, while the smaller ice fragments quickly dis-  
 503 perse (Figure 2). The tabular iceberg drifts towards the north east, driven by the wind  
 504 and steered by the Coriolis force. As the tabular iceberg drifts northwards, it rotates in  
 505 a counterclockwise direction (the direction of the Coriolis force in the Southern Hemis-  
 506 phere), and makes contact with the eastern boundary of the domain, before continu-  
 507 ing northward. Most of the smaller ice fragments also move to the northeast, but not  
 508 as a cohesive unit. Some of these element also move to other parts of the domain.

509 The direction (and speed) of the iceberg drift is largely determined by the wind speed  
 510 and direction. Perturbation experiments using different wind stresses show that for suf-  
 511 ficiently large winds, the tabular iceberg drifts to the north east when  $\tau_x > 0$ , and to  
 512 the north west when  $\tau_x < 0$  (not shown). For a purely zonal wind stress with  $|\tau_x| \leq$   
 513  $0.01 \frac{N}{m^2}$ , the iceberg does not move away from the ice shelf. When the wind is purely off-  
 514 shore ( $\tau_x = 0.0 \frac{N}{m^2}$ ), a meridional wind stress  $\tau_y \geq 0.05 \frac{N}{m^2}$  is needed to move the tab-  
 515 ular iceberg away from the ice shelf. While this result is partly an artifact of the cho-  
 516 sen shape of the calving iceberg, it is also consistent with Bassis and Jacobs [2013] who  
 517 noted that calving is a two step process consisting of (i) ice-shelf rifting that forms an  
 518 iceberg and (ii) iceberg detachment. The results here suggest that strong (cross-shore)  
 519 winds may be required to drive large tabular icebergs away from their source ice shelves.

520 **4.2 Breaking bonds**

521 The numerical bonds in the iceberg model enable the tabular iceberg to retain its  
 522 shape. This is demonstrated by comparing the Control simulation to an identical sim-  
 523 ulation where all numerical bonds have been removed (Figure 9, movie S5). In the bond-  
 524 free simulation, the ice elements disperse and the calved iceberg quickly loses its orig-  
 525 inal structure. This bond-free simulation does not adequately represent tabular iceberg,  
 526 which can move long distances through the ocean as a cohesive unit. This result moti-  
 527 vates the inclusion of bonds in the iceberg model, even though they are more compu-  
 528 tationally expensive than traditional point-iceberg models.

529 By breaking some (but not all) numerical bonds, we can simulate breaking of tab-  
 530 ular icebergs into smaller pieces. Figure 10 shows the results of an experiment which is  
 531 identical to the Control experiment, except that all numerical bonds that intersect the  
 532 line  $x = \frac{L_x}{2}$  have also been severed. This effectively cuts the large tabular iceberg into

533 two halves. As the icebergs drift northwards, the two halves of the tabular iceberg each  
 534 move as a cohesive unit, but they are able to move independently of one other (Figure  
 535 10, movie S2). The two large fragments initially move together, but begin to separate  
 536 after a few days. The breaking of a tabular iceberg has the additional effect of increas-  
 537 ing the total surface area of ice exposed to the ocean, thus increasing the total decay rate  
 538 of the icebergs.

### 539 4.3 Ocean response

540 Since the tabular iceberg is submerged in the ocean, the iceberg calving and drift  
 541 affects the surrounding ocean. In the Control simulation, as the tabular iceberg drifts  
 542 northward a warming of the surface waters is observed around the tabular iceberg, with  
 543 the largest warming occurring at the ice-shelf front and along the tabular iceberg's rounded  
 544 edge (Figure 2). This surface warming is caused by upwelling of the warmer waters from  
 545 beneath the ice shelf and iceberg. As the icebergs drifts away from the ice shelf, these  
 546 warmer waters remain at the surface, mapping out the iceberg wake (Figure 2). The mo-  
 547 tion of the tabular iceberg disturbs the ocean surface, which affects ocean velocities through  
 548 out the water column (Figure 11). The elevated shears around the tabular iceberg lead  
 549 to increased vertical mixing in the vicinity of the iceberg, which alters the stratification  
 550 of the water column (Figure 8), warming the upper ocean. The signature of upwelling  
 551 water in the wake of a drifting tabular iceberg bears some similarity to satellite obser-  
 552 vations of streaks of increased ocean color in the wake of tabular iceberg in the South-  
 553 ern Ocean [Duprat et al, 2016], suggesting that the increased productivity around ice-  
 554 bergs may be driven by upwelling water delivering nutrients to the surface.

### 555 4.4 Iceberg melt rates

556 The increased subsurface velocities and temperatures cause elevated melt rates at  
 557 the base of the ice shelf and iceberg (Figure 12). The largest melt rates are observed at  
 558 the newly calved ice-shelf front and on the rounded side of the tabular iceberg (Figure  
 559 12a), where the iceberg calving has created steep ice cliffs. These sharp ice fronts allow  
 560 for large ocean currents (Figure 12c), which drive the elevated melt rates. The elevated  
 561 melt rates act to smooth out the ice front over time, making the ice cliff less steep. While  
 562 this is likely a real phenomena that could be observed in nature, we should be wary of  
 563 the modeled velocities at the ice cliffs, since large changes in ice thicknesses are associ-  
 564 ated with numerical pressure gradient errors which can drive spurious motion.

565 The large melt rates along the ice edges are also partly driven by the fact that dif-  
 566 ferent melt parametrization are used in the interior and edges of large ice structures (see  
 567 Section 2.5). Figure 13 shows the melt rates computed with (a) the 3-equation-model  
 568 parametrization [Holland and Jenkins, 1999], (b) point-particle-iceberg-melt parametriza-  
 569 tion [Gladstone et al, 2001], and (c) the mixed-melt-rate parametrization (introduced  
 570 in Section 2.5). The 3-equation-model melt rates (Figure 13a) are less than a third of  
 571 the size of those calculated using the point-particle-iceberg-melt parametrization (Fig-  
 572 ure 13b). When the mixed-melt-rate parametrization is used (Figure 13c), the very high  
 573 melt rates are only observed at the edges of ice structures.

## 574 5 Summary

575 In this study we present a novel framework for simulating tabular icebergs in ocean  
 576 models, and representing icebergs with finite extent and structure **submerged in the ocean**.  
 577 In this framework, large tabular icebergs are represented by collections of Lagrangian  
 578 elements that are held together by numerical bonds. Each ice element is assigned a sur-  
 579 face area and shape, and can interact with the ocean and other elements in a way which  
 580 is consistent with the shape of the element. Such a representation allows tabular icebergs

581 to interact with the ocean across a wide area (larger than a grid cell), and individual ice  
 582 elements to behave as if they had a finite extent. This is in contrast to previous repre-  
 583 sentations of icebergs in numerical models [Jongma et al, 2009; Martin and Adcroft, 2010;  
 584 Marsh et al, 2015] that treat icebergs as point particles. Assigning a finite extent to el-  
 585 ements prevents icebergs from piling up on top of one another, which has been an issue  
 586 for previous point-particle iceberg models. Explicitly resolving tabular icebergs in the  
 587 ocean allows the icebergs **to be non-levitating and thus** to interact with the ocean in a  
 588 more realistic way, and allows us to study the effects that tabular icebergs have on ocean  
 589 circulation. Including numerical bonds between elements allows for simulations which  
 590 emulate iceberg calving and fracture by severing the bonds.

591 The capabilities of the tabular iceberg model are demonstrated by modeling a tab-  
 592 ular iceberg drifting away from an idealized ice shelf (also constructed using Lagrangian  
 593 elements). The results show that explicitly resolving tabular icebergs in the ocean al-  
 594 lows for a complex interaction between the iceberg and the surrounding ocean. In our  
 595 Control setup, a tabular iceberg is driven away from the ice shelf by ocean currents, wind  
 596 stress, and the Coriolis force. As the iceberg moves through the water, it disturbs the  
 597 ocean surface, driving ocean currents. The motion of the iceberg and melt beneath the  
 598 iceberg drive upwelling along the sides of the iceberg, which entrains ambient water and  
 599 causes a warming of the surface ocean in the wake of the iceberg. The changing ocean  
 600 conditions feed back onto the iceberg, affecting its motion and melt rates. The highest  
 601 melt rates are observed at edge of the iceberg which has the steepest ice cliff. These have  
 602 the effect of smoothing out the ice edge over time. Simulations without using numeri-  
 603 cal bonds showed that the bonds are essential for allowing the iceberg to move as a unit.  
 604 We also demonstrate that by breaking these numerical bonds we can simulate iceberg  
 605 fracture, which is important process that increases the rate of iceberg decay.

606 To our knowledge, the model presented in this study is the first model to explic-  
 607 itly resolve drifting tabular icebergs in an ocean model that can be used for climate stud-  
 608 ies. A natural extension of this work is a representation of tabular icebergs in a general  
 609 circulation model (GCM). However, before this can be done, there are a number of is-  
 610 sues that need to be resolved: firstly, the question of how and when to introduce tab-  
 611 ular icebergs into the ocean needs to be addressed. For GCM's with active ice shelves,  
 612 a calving law is needed to release the tabular iceberg into the ocean. The question of what  
 613 calving law to use is a topic of ongoing research [Benn et all, 2007; Alley et al, 2008; Lev-  
 614 ermann et al, 2012; Bassis and Jacobs, 2013] and is still unresolved. One potential way  
 615 to temporarily bypass this problem would be to run hindcast simulations using histor-  
 616 ically observed calving events. A related issue is the question of how and when to break  
 617 the bonds within the freely floating icebergs to simulate iceberg breakup. Without a rule  
 618 for iceberg breakup, the tabular icebergs would likely drift to unrealistically low latitudes.  
 619 Further work is also needed to understand (and model) the interactions between tab-  
 620 ular icebergs and sea ice, and to parametrize the effects of iceberg grounding, as these  
 621 interactions play a large role in dictating the trajectories of tabular icebergs. However,  
 622 despite these remaining challenges, the technical framework described in this article is  
 623 potentially a useful step towards including tabular icebergs in global GCM's.

## 624 6 Appendix A

### 625 6.1 Environmental forces on ice elements

626 The non-interactive forces on an ice element are as described in [Martin and Ad-  
 627 croft, 2010], and are repeated here for completeness. **For these non-interactive forces, the**  
 628 **elements are assumed to be cuboids with time-evolving lengths, widths and thicknesses.**  
 629 The forces on an element due to air (a), ocean (o) and sea ice (si) drag are given by

$$(624) \vec{F}_a = \rho_a (0.5 c_{a,v} WF + c_{a,h} LW) |\vec{u}_a - \vec{u}| (\vec{u}_a - \vec{u}), \quad (11)$$

$$(\vec{\bar{F}}_o) = \rho_o(0.5c_{o,v}W(D - T_{si})F + c_{o,h}LW)|\vec{u}_o - \vec{u}|(\vec{u}_o - \vec{u}), \quad (12)$$

$$(\vec{F}_{si}) = \rho_{si}(0.5c_{si,v}WT_{si}F + c_{si,h}LW)|\vec{u}_{si} - \vec{u}|(\vec{u}_{si} - \vec{u}). \quad (13)$$

Here  $\rho_a$ ,  $\rho_o$ ,  $\rho_{si}$ , are the density of air, ocean and sea ice, respectively.  $c_{a,v}$ ,  $c_{o,v}$  and  $c_{si,v}$  are the vertical drag coefficients with air, ocean and sea ice, while  $c_{a,h}$ ,  $c_{o,h}$  and  $c_{si,h}$  are the respective horizontal drag coefficients.  $\vec{u}_a$ ,  $\vec{u}_o$ ,  $\vec{u}_{si}$ , are the velocities of air, ocean and sea ice, respectively. L, W, T, F and D are the length, width, thickness, freeboard, and draft of the ice element. The element thickness is related to the draft and freeboard by  $T = F + D$  and  $D = \frac{\rho}{\rho_o}T$ , where  $\rho$  is the ice element density.  $T_{si}$  is the sea ice thickness.

The wave radiation force ( $\vec{F}_R$ ) is given by

$$\vec{F}_R = \rho_o c_r g a \frac{WL}{W+L} \frac{\vec{v}_a}{|\vec{v}_a|} \min(a, F) \quad (14)$$

where  $g$  is the acceleration due to gravity,  $a$  is the wave amplitude empirically related to the wind speed by  $a = 0.010125|\vec{v}_a - \vec{v}_o|$ , and  $c_{wd}$  is the wave drag coefficient defined as

$$c_{wd} = 0.06 \min\left(\max\left[0, \frac{L - L_c}{L_t - L_c}\right], 1\right), \quad (15)$$

where  $L_w = 0.32|\vec{v}_a - \vec{v}_o|^2$  is an empirical wave length,  $L_c = 0.125L_w$  is the cutoff length, and  $L_t = 0.25L_w$  is the upper limit.

The pressure gradient force is approximated as a force due to sea surface slope and given by

$$\vec{F}_{SS} = -Mg\vec{\nabla}\eta \quad (16)$$

where  $\eta$  is the sea surface height.

## 6.2 Melt rate parametrization

As discussed in Section 2.5, unbounded ice elements in the iceberg model decay according to parameterizations for iceberg decay typically used in iceberg drift models [Martin and Adcroft, 2010], while ice elements within larger ice structures have only a basal melt given by the three equation model [Holland and Jenkins, 1999].

For unbonded ice elements, the element thickness decays due to basal melt at a rate  $M_b$ , while the length and width of the elements decay as a result of melt due to wave erosion,  $M_e$ , and melt due to buoyant convection,  $M_v$ . Following Gladstone et al [2001] and Martin and Adcroft [2010], the basal melt rate, the 'melt' due to wave erosion wave erosion melt rate, and buoyant convection melt rate are parameterized by

$$M_b = 0.58 |\vec{v} - \vec{v}_0|^{0.8} \frac{\tilde{T}_0 - \tilde{T}}{L^{0.2}} \quad (17)$$

$$M_e = \frac{1}{12} S_s \left( 1 + \cos [\pi A_i^3] \right) \left( \tilde{T}_0 + 2 \right), \quad (18)$$

$$M_v = \left( 7.62 \times 10^{-3} \right) \tilde{T}_0 + \left( 1.29 \times 10^{-3} \right) \tilde{T}_0^2. \quad (19)$$

$\tilde{T}$  is the effective iceberg temperature and is set to  $\tilde{T} = -4^\circ\text{C}$ ,  $\tilde{T}_0$  is the temperature at the top of the ocean,  $A_i$  is the sea-ice area fraction, and  $S_s$  is the sea state, which is given by the Beaufort scale

$$S_s = \frac{2}{3} |\vec{u}_a - \vec{u}_o|^{\frac{1}{2}} + \frac{1}{10} |\vec{u}_a - \vec{u}_o| \quad (20)$$

663 All three melt rates are in units of meters per day.

664 For elements inside larger structures, the melt due to wave erosion and melt due  
 665 to buoyant convection are set to zero, and the basal melt,  $M_s$ , is given by the standard  
 666 three equation model [Holland and Jenkins, 1999].

## 667 7 Appendix B

### 668 7.1 Modified Verlet Algorithm

669 The model uses a version velocity Verlet time-stepping algorithm, which has been  
 670 modified to allow part of the forcing to be calculated implicitly. The traditional veloc-  
 671 ity Verlet algorithm is commonly used in molecular dynamics, as it is simple to imple-  
 672 ment, second order accurate and computationally efficient [Swope et al, 1982; Omelyan  
 673 et al, 2002]. Here we modify the traditional scheme to allow for the drag forces to be mod-  
 674 elled implicitly, which prevents large accelerations for element's **elements** whose mass ap-  
 675 proaches zero. To do this, we include both an implicit and explicit acceleration,  $a = a^{exp} +$   
 676  $a^{imp}$ . The explicit acceleration,  $a^{exp}$ , includes all forcing terms which depend only on  
 677 the previous time step and the current position, while the implicit acceleration,  $a^{imp}$ ,  
 678 includes forcing terms which depend on the velocity at the current time step (in partic-  
 679 ular the drag and Coriolis forces).

680 Using a time step of  $\Delta t$ , and subscripts to denote the time step (so that  $t_{n+1} =$   
 681  $t_n + \Delta t$ ), the modified velocity Verlet scheme can be written as:

- 682 1) Calculate updated position:  $x_{n+1} = x_n + u_n \Delta t + \frac{\Delta t^2}{2} \left( a_n^{exp} + a_n^{imp} \right)$ .
- 683 2) Calculate  $a_{n+1}^{exp}$
- 684 3) Calculate  $a_{n+1}^{imp}$  and  $u_{n+1} = u_n + \frac{\Delta t}{2} \left( a_n^{exp} + a_{n+1}^{exp} \right) + (\Delta t) a_{n+1}^{imp}$

685 This scheme reduces to the traditional velocity Verlet when  $a^{imp}$  is set to zero. Note  
 686 that  $a_{n+1}^{exp} = a_{n+1}^{exp}(x_{n+1}, t_n)$  is an explicit function of  $x_{n+1}$  and other quantities eval-  
 687 uated at time  $t_n$ , while  $a_{n+1}^{imp} = a_{n+1}^{imp}(u_{n+1}, x_{n+1}, t_n)$  additionally depends on  $u_{n+1}$ , and  
 688 needs to be solved implicitly. For this reason in step three,  $a_{n+1}^{imp}$  and  $u_{n+1}$  need to be  
 689 solved simultaneously, as described in the next subsection.

690 In equation (1), the forces due to ocean drag, atmospheric drag and sea ice drag  
 691 are treated implicitly. The force due to sea surface slope and wave radiation are treated  
 692 explicitly. The Coriolis term is handled using the Crank-Nicolson scheme so that half  
 693 of the effect is implicit and half is explicit. The elastic part of the interactive forces is  
 694 treated explicitly, while the interactive damping is handled semi-implicitly in that the  
 695 drag force on element A by element B depends on the velocities of elements A and B eval-  
 696 uated at time  $t_{n+1}$  and  $t_n$ , respectively.

### 697 7.2 Solving for the velocity implicitly

698 Since this modified scheme contains some forcing terms which are handled implic-  
 699 itly,  $a_{n+1}^{imp}$  and  $u_{n+1}$  need to be calculated simultaneously. We demonstrate how this is  
 700 done, using a simplified one-dimensional version of equation (1), neglecting the atmo-  
 701 spheric drag, sea ice drag and Coriolis force, so that the only implicitly treated term is  
 702 the ocean drag. In this demonstration, we use a superscript to denote the ocean drag  
 703 force,  $F^o$ , and ocean velocity,  $u^o$ , to avoid confusion with the subscripts indicating time  
 704 step. We also define an explicit force,  $F^{exp}$ , which accounts for all forces not proportional  
 705 to the element velocity. With these simplifications, the implicit and explicit accelerations  
 706 are

$$a^{exp} = \frac{1}{M} (\vec{F}^{exp}) \quad (21)$$

707

$$a^{imp} = \frac{1}{M}(F^o) \quad (22)$$

708

The ocean drag force at time  $t_{n+1}$  is modeled (mostly) implicitly as

$$F_{n+1}^o = \tilde{c}^o |u_n^o - u_n| (u_n^o - u_{n+1}), \quad (23)$$

709

where  $\tilde{c}^o$  is the effective drag coefficient, accounting for the dimensions of the ice element (see equation 12).

711

Step 3 of the modified velocity Verlet scheme can be rewritten by introducing an intermediate velocity  $u^*$ , which only depends on the velocity and acceleration at time  $t_n$ ,

$$u_n^* = u_n + \frac{1}{2}(\Delta t)a_n^{exp}. \quad (24)$$

714

Using this, the updated velocity (Step 3) can be written

$$u_{n+1} = u_n^* + \frac{\Delta t}{2}a_{n+1}^{exp} + (\Delta t)a_{n+1}^{imp}. \quad (25)$$

715

Including the forcing terms into this equations gives

$$u_{n+1} = u_n^* + \frac{\Delta t}{2M}(F_{n+1}^{exp}) + \frac{\Delta t}{M} \left( c_w |u_n^o - u_n| (u_n^o - u_{n+1}) \right) \quad (26)$$

716

Solving for  $u(t_{n+1})$  in terms of quantities which only depend on the previous time step gives

$$u_{n+1} = \frac{u_n^* + \frac{\Delta t}{2M}(F_{n+1}^{exp}) + \frac{\Delta t}{M} \left( c_w |u_n^o - u_n| (u_n^o) \right)}{\left( 1 + \frac{\Delta t}{M} c_w |u_n^o - u_n| \right)} \quad (27)$$

718

Once the  $u_{n+1}$  has been found, it can be used to calculate the explicit and implicit accelerations, which are required for the next time step.

720

Finally, we note that the the drag term (equation 23) is not entirely implicit, since the element velocity inside the absolute value is evaluated at time  $t_n$ , rather than at time  $t_{n+1}$ . This is done so that we can solve for the updated velocity analytically. One consequence of this is that it can give rise to a small oscillation in the element velocity. This oscillation is addressed by using a predictive corrective scheme: after solving for a first guess of the velocity at time  $t_{n+1}$ , this estimate of the velocity is used to update the estimate of the drag force (i.e.: inside the absolute value signs). This updated drag, can now be used to repeat the process described above to find an improved estimate of the velocity. We found that two iterations were sufficient to remove the unwanted oscillation.

730

The procedure described in this section is easily extended to include more forcing terms and two dimensions (where it involves inverting a  $2 \times 2$  matrix).

732

## 8 Appendix C

733

### Connecting bonds across processor boundaries

734

Since the model is parallelized across multiple processors, it often happens that two elements on different processes are bonded together. Keeping track of numerical bonds across processor boundaries requires a lot of book keeping. In this section we describe the how the model handles bonds across processor boundaries.

738        The basics of the bond bookkeeping work as follows: consider an element A and  
 739        an element B that are bonded together. Each element has a copy of the bond (a piece  
 740        of memory which describes the bond between the two elements), which is stored with  
 741        the element. Let A-B be the bond stored by element A, and B-A be the bond stored by  
 742        element B. Bond A-B contains a pointer which points to element B and bond B-A con-  
 743        tains a pointer which points to element A.

744        Consider a situation where element A and B are originally on Processor 1, and then  
 745        element B moves to Processor 2. When this occurs, the memory assigned to element B  
 746        on processor 1 is removed, and is allocated on Processor 2. This means that the pointer  
 747        to element B in bond A-B (stored in element A on Processor 1) is no longer assigned.  
 748        Similarly, the pointer to element A in bond B-A (stored in element B on Processor 2)  
 749        is no longer assigned. Before the next time step, a halo update occurs, so that the there  
 750        is a copy of element A in the halo of Processor 2 and a copy of element B in the halo of  
 751        Processor 1. After the halo update, the bonds A-B and B-A have to be reconnected on  
 752        both Processor 1 and 2. To aid in reconnecting the bonds, a copy of the grid cell num-  
 753        ber of element B is stored in the bond A-B and a copy of the grid cell number of element  
 754        A is stored in the bond B-A. We refer to this as the ‘most recent address’. Before a bond  
 755        is moved from one processor to another, the ‘most recent address’ is updated, so that  
 756        the bond can be reconnected later. To reconnect bond A-B on Processor 1 (for exam-  
 757        ple), we find the most recent address of element B, and search through the list of ele-  
 758        ments in the grid cell corresponding to the most recent address of element B until ele-  
 759        ment B is found. The pointer to element B in bond A-B is reassigned, and the bond is  
 760        said to be connected.

761        The reconnected bond A-B (stored in element A) is said to be working properly  
 762        when the following four tests pass:

- 763        1. The pointer to element B is assigned on bond A-B.
- 764        2. The corresponding bond B-A exists on element B.
- 765        3. A pointer to element A exists in this bond B-A.
- 766        4. The element A which is being pointed to is the same element A where you started.

767        A useful tool for debugging the disconnecting and reconnecting bonds routines is that  
 768        each element is assigned a unique number so that elements are easily identified.

769 **Acknowledgments**

770 This study is supported by awards NA08OAR4320752 and NA13OAR439 from the Na-  
771 tional Oceanic and Atmospheric Administration, U.S. Department of Commerce. Spe-  
772 cial thanks to Robert Hallberg who contributed to this study through many helpful con-  
773 versations. The statements, findings, conclusions, and recommendations are those of the  
774 authors and do not necessarily reflect the views of the National Oceanic and Atmospheric  
775 Administration, or the U.S. Department of Commerce. The simulations in this paper  
776 can be reproduced using the model code and experimental setups found at [https://github.com/sternalon/Iceberg\\_repo](https://github.com/sternalon/Iceberg_repo)

777 **References**

- 778 Asay-Davis, X. S., S. L. Cornford, B. K. Galton-Fenzi, R. M. Gladstone, G. H. Gud-  
 779 mundsson, D. M. Holland, P. R. Holland, and D. F. Martin (2016), Experimental  
 780 design for three interrelated marine ice sheet and ocean model intercomparison  
 781 projects: MISMIP v. 3 (MISMIP+), ISOMIP v. 2 (ISOMIP+) and MISOMIP v. 1  
 782 (MISOMIP1). *Geoscientific Model Development* 9, no. 7: 2471.
- 783 Arrigo, K. R., G. L. van Dijken, D. G. Ainley, M. A. Fahnestock, and T. Markus  
 784 (2002). Ecological impact of a large Antarctic iceberg. *Geophys. Res. Lett.*, 29(7).
- 785 Alley, R. B., H. J. Horgan, I. Joughin, K. M. Cuffey, T. K. Dupont, B. R. Parizek,  
 786 S. Anandakrishnan, and J. Bassis (2008), A simple law for ice-shelf calving. *Sci-  
 787 ence* 322, no. 5906, 1344-1344.
- 788 Bassis, J. N., and S. Jacobs (2013), Diverse calving patterns linked to glacier geom-  
 789 etry. *Nature Geoscience*, 6(10), 833-836.
- 790 Benn, D. I., C. R. Warren, and R. H. Mottram (2007). Calving processes and the  
 791 dynamics of calving glaciers. *Earth-Science Reviews*, 82(3), 143-179.
- 792 Bigg, G. R., Wadley, M. R., Stevens, D. P., and Johnson, J. A. (1997), Modeling the  
 793 dynamics and thermodynamics of icebergs. *Cold Regions Science and Technology*,  
 794 26(2), 113-135.
- 795 Borstad, C. P., A. Khazendar, E. Larour, M. Morlighem, E. Rignot, M. P. Schodlok,  
 796 and H. Seroussi (2012), A damage mechanics assessment of the Larsen B ice shelf  
 797 prior to collapse: Toward a physically-based calving law, *Geophys. Res. Lett.*, 39,  
 798 L18502
- 799 Biddle, L. C., J. Kaiser, K. J. Heywood, A. F. Thompson and A. Jenkins (2015),  
 800 Ocean glider observations of iceberg-enhanced biological productivity in the north-  
 801 western Weddell Sea, *Geophys. Res. Lett.*, 42, 459465.
- 802 De Rydt, J., and G. H. Gudmundsson (2016), Coupled ice shelf ocean modeling and  
 803 complex grounding line retreat from a seabed ridge. *J. of Geophys. Res.: Earth  
 804 Surface*, 121(5), 865-880.
- 805 Dunne, J.P., J.G. John,, A.J. Adcroft, S.M. Griffies, R.W. Hallberg, E. Shevliakova,  
 806 R.J. Stouffer, W. Cooke, K.A. Dunne, M.J Harrison, and J.P. Krasting (2012),  
 807 GFDL's ESM2 global coupled climate-carbon Earth System Models. Part I: Phys-  
 808 ical formulation and baseline simulation characteristics. *J. of Climate*, 25(19),  
 809 6646-6665.
- 810 Depoorter, M. A., J. L. Bamber, J. A. Griggs, J. T. M. Lenaerts, Stefan RM Ligten-  
 811 berg, M. R. van den Broek, and G. Moholdt (2013), Calving fluxes and basal melt  
 812 rates of Antarctic ice shelves. *Nature*, 502(7469), 89-92.
- 813 Determan J., Gerdes R. (1994), Melting and freezing beneath ice shelves: impli-  
 814 cations from a three-dimensional ocean-circulation model. *Ann. Glaciol.*, 20,  
 815 413-419.
- 816 Dowdeswell, J. A., and J. L. Bamber (2007), Keel depths of modern Antarctic ice-  
 817 bergs and implications for sea-floor scouring in the geological record. *Marine  
 818 Geology*, 243(1), 120-131.
- 819 Duprat, L. P., G. R. Bigg, and D. J. Wilton (2016), Enhanced Southern Ocean  
 820 marine productivity due to fertilization by giant icebergs. *Nature Geoscience*.
- 821 Eckert, E. R. G. (1950). Introduction to the Transfer of Heat and Mass. McGraw-  
 822 Hill.
- 823 Fogwill, C.J., E. van Sebille, E.A. Cougnon, C.S. Turney, S.R. Rintoul, B.K. Galton-  
 824 Fenzi, G.F. Clark, E.M. Marzinelli, E.B. Rainsley, and L. Carter (2016), Brief  
 825 communication: Impacts of a developing polynya off Commonwealth Bay, East  
 826 Antarctica, triggered by grounding of iceberg B09B. *The Cryosphere*, 10(6),  
 827 p.2603.
- 828 Gladstone, R. M., G. R. Bigg, and K. W. Nicholls. (2001), Iceberg trajectory mod-  
 829 eling and meltwater injection in the Southern Ocean (19782012). *J. of Geophys.*

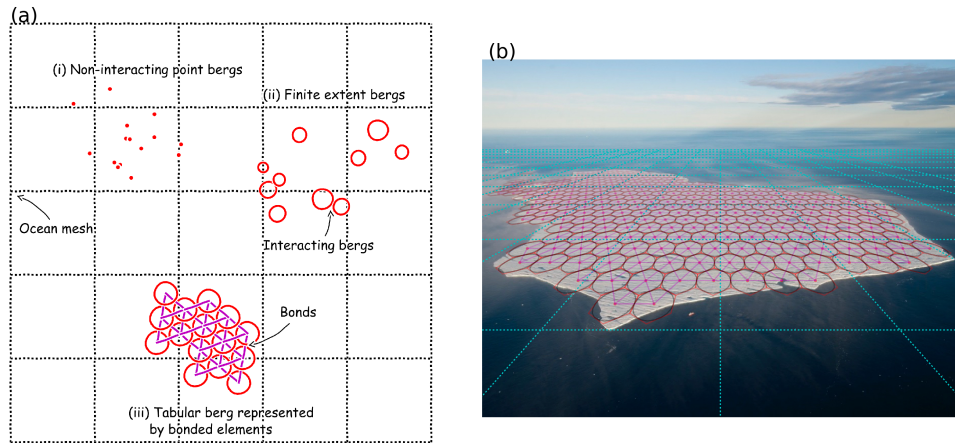
- 830      *Res.: Oceans*, 106(C9), 19903-19915.
- 831      Goldberg, D. N., C. M. Little, O. V. Sergienko, A. Gnanadesikan, R. Hallberg, and  
832      M. Oppenheimer (2012), Investigation of land ice/ocean interaction with a fully  
833      coupled ice-ocean model: 1. Model description and behavior. *J. of Geophys. Res.:  
834      Earth Surface*, 117(F2).
- 835      Gladish, C. V., D. M. Holland, P. R. Holland, and S. F. Price (2012), Ice-shelf basal  
836      channels in a coupled ice/ocean model. *J. of Glaciol.*, 58(212), 1227-1244.
- 837      Grosfeld K., R. Gerdes, J. Determan (1997), Thermohaline circulation and interac-  
838      tion between ice shelf cavities and the adjacent open ocean. *J. Phys. Oceanogr.*,  
839      **102**, C7, 15959-15610.
- 840      Grosfeld, K., and H. Sandhger, (2004). The evolution of a coupled ice shelfocean sys-  
841      tem under different climate states. *Global and Planetary Change*, 42(1), 107-132.
- 842      Hallberg, R., A. Adcroft, J. P. Dunne, J. P., Krasting, R. J., and Stouffer (2013),  
843      Sensitivity of twenty-first-century global-mean steric sea level rise to ocean model  
844      formulation. *J. of Climate*, 26(9), 2947-2956.
- 845      Holland D. M., Jenkins A. (2001), Adaptation of an isopycnic coordinate ocean  
846      model for the study of circulation beneath ice shelves. *Mon. Wea. Rev.*, 129, 1905-  
847      1927.
- 848      Holland P. R. and D. L. Feltham (2006), The effects of rotation and ice shelf topog-  
849      raphy on frazil-laden Ice Shelf Water plumes. *J. Phys. Oceanogr.*, 36, 2312-2327.
- 850      Holland, D. M., and A. Jenkins (1999), Modeling thermodynamic ice-ocean interac-  
851      tions at the base of an ice shelf. *J. of Phys. Oceanogr.* 29.8, 1787-1800.
- 852      Hellmer H.H., Olbers D. J. (1989), A two-dimensional model for the thermohaline  
853      circulation under an ice shelf. *Antarctic Science*, 1, 325- 336.
- 854      Henderson J., J. S. P. Loe (2016), The Prospects andChallenges for Arctic Oil De-  
855      velopment. *Oil, Gas and Energy Law Journal (OGEL)*, 14 (2)
- 856      Hopkins, M. A. (1996). On the mesoscale interaction of lead ice and floes. *J. of  
857      Geophys. Res.: Oceans*, 101(C8), 18315-18326.
- 858      Hopkins, M. A. (2004). A discrete element Lagrangian sea ice model. *Engineering  
859      Computations*, 21(2/3/4), 409-421.
- 860      Hunke, Elizabeth C., and Darin Comeau (2011), Sea ice and iceberg dynamic inter-  
861      action. *J. of Geophys. Res.: Oceans* 116, C5.
- 862      Gaskill, H. S., and J. Rochester (1984). A new technique for iceberg drift prediction.  
863      *Cold Reg. Sci. Technol.*, 8(3), 223-234.
- 864      Jacobs, S. S., H. H. Helmer, C. S. M. Doake, A. Jenkins, R. M. Frolich (1992), Melting  
865      of ice shelves and the mass balance of Antarctica. *J. of Glaciol.*, 38(130),  
866      375-387.
- 867      Jakobsen, T. (2001). Advanced character physics. *In Game Developers Conference*,  
868      Vol. 3.
- 869      Jenkins, A., P. Dutrieux, S. S. Jacobs, S. D. McPhail, J. R. Perrett, A. T. Webb,  
870      and D. White (2010), Observations beneath Pine Island Glacier in West Antarc-  
871      tica and implications for its retreat. *it Nature Geo.*, 3(7), 468-472.
- 872      Jacobs, S. S., A. Jenkins, C. F. Giulivi, and P. Dutrieux (2011). Stronger ocean cir-  
873      culation and increased melting under Pine Island Glacier ice shelf. *Nature Geo.*,  
874      4(8), 519-523.
- 875      Jongma, J. I., E. Driesschaert, T. Fichefet, H. Goosse, and H. Renssen (2009), The  
876      effect of dynamic-thermodynamic icebergs on the Southern Ocean climate in a  
877      three-dimensional model, *Ocean Modell.*, 26, 104113.
- 878      Kubat I., M. Sayed, S. Savage, T. Carrieres (2005), An operational model of iceberg  
879      drift *Int. J. Off. Polar Eng.*, 15 (2), 125131
- 880      Lewis E.L. and R.G. Perkin (1986), Ice pumps and their rates. *J. of Geophys. Res.*,  
881      91, 11756-11762.
- 882      Losch, M. (2008). Modeling ice shelf cavities in a z coordinate ocean general circula-  
883      tion model. *J. of Geophys. Res.: Oceans*, 113(C8).

- 884 Li, B., H. Li, Y. Liu, A. Wang and S. Ji (2014), A modified discrete element model  
 885 for sea ice dynamics. *Acta Oceanologica Sinica*, 33(1), 56-63.
- 886 Liu, M. B. and G. R. Liu (2010), Smoothed particle hydrodynamics (SPH): an  
 887 overview and recent developments. *Archives of computational methods in engineering*,  
 888 17(1), 25-76.
- 889 Lichéy, C., and H. H. Hellmer (2001). Modeling giant-iceberg drift under the influence  
 890 of sea ice in the Weddell Sea, Antarctica. *J. of Glaciol.*, 47(158), 452-460.
- 891 Levermann, A., T. Albrecht, R. Winkelmann, M. A. Martin, M. Haseloff, and I.  
 892 Joughin. (2012), Kinematic first-order calving law implies potential for abrupt  
 893 ice-shelf retreat. *The Cryosphere*, 6(2), 273-286.
- 894 Mountain, D. G. (1980). On predicting iceberg drift. *Cold Reg. Sci. Technol.*, 1(3-4),  
 895 273-282.
- 896 Martin, T., and Adcroft, A. (2010), Parameterizing the fresh-water flux from land  
 897 ice to ocean with interactive icebergs in a coupled climate model. *Ocean Modelling*,  
 898 34(3), 111-124.
- 899 Marsh, R., V. O. Ivchenko, N. Skliris, S. Alderson, G. R. Bigg, G. Madec, A. T.  
 900 Blaker Y. Aksenov, B. Sinha, A.C. Coward, and J.L. Sommer (2015), NEMOICB  
 901 (v1. 0): interactive icebergs in the NEMO ocean model globally configured at  
 902 eddy-permitting resolution. *Geoscientific Model Development* 8, no. 5 (2015):  
 903 1547-1562.
- 904 MacAyeal D.R. (1984), Thermohaline Circulation Below the Ross Ice Shelf: A Con-  
 905 sequence of Tidally Induced Vertical Mixing and Basal Melting. *J. Geophys. Res.*,  
 906 89, 597-606
- 907 Merino, N., Le Sommer, J., Durand, G., Jourdain, N. C., Madec, G., Mathiot, P.,  
 908 and Tournadre, J. (2016), Antarctic icebergs melt over the Southern Ocean: cli-  
 909 matology and impact on sea ice. *Ocean Modelling*, 104, 99-110.
- 910 Nicholls K.W. (1996), Temperature variability beneath Ronne Ice Shelf, Antarctica,  
 911 from thermistor cables. *J. Phys. Oceanogr.*, 11, 1199-1210.
- 912 Nicholls KW, Østerhus S, Makinson K (2009), Ice-Ocean processes over the con-  
 913 tinental shelf of the southern Weddell Sea, Antarctica: a review. *Rev. Geophys.*  
 914 47(3).
- 915 Omelyan, I. P., M. I. Mryglod, and R. Folk (2002), Optimized Verlet-like algorithms  
 916 for molecular dynamics simulations. *Physical Review E*, 65(5), 056706.
- 917 Pizzolato, L., S. E. Howell, C. Derksen, J. Dawson, L. Copland (2014), Changing  
 918 sea ice conditions and marine transportation activity in Canadian Arctic waters  
 919 between 1990 and 2012, *Climatic Change* 123 (2), 161173.
- 920 Pan, W., A. M. Tartakovsky, and J. J. Monaghan (2013). Smoothed particle hydro-  
 921 dynamics non-Newtonian model for ice-sheet and ice-shelf dynamics. *J. of Comp.  
 922 Phys.*, 242, 828-842.
- 923 Pralong, A., and M. Funk (2005), Dynamic damage model of crevasse opening and  
 924 application to glacier calving, *J. Geophys. Res.*, 110, B01309.
- 925 Rabatel, M., S. Labb and J. Weiss (2015), Dynamics of an assembly of rigid ice  
 926 floes. *J. of Geophys. Res.: Oceans*, 120(9), 5887-5909.
- 927 Rackow, T., C. Wesche, R. Timmermann, H. H. Hellmer, S. Juricke and T.  
 928 Jung (2017), A simulation of small to giant Antarctic iceberg evolution: dif-  
 929 ferential impact on climatology estimates. *J. of Geophys. Res.: Oceans*, doi:  
 930 10.1002/2016JC012513
- 931 Rignot, E., S. Jacobs, J. Mouginot, and B. Scheuchl (2013), Ice-shelf melting around  
 932 Antarctica. *Science*, 341, no. 6143 (2013): 266-270.
- 933 Robinson, N. J., M. J. M. Williams, P. J. Barrett, and A. R. Pyne (2010), Observa-  
 934 tions of flow and ice-ocean interaction beneath the McMurdo Ice Shelf, Antarctica,  
 935 *J. Geophys. Res.*, 115, C03025
- 936 Sergienko, O. V. (2013). Basal channels on ice shelves. *J. of Geophys. Res.: Earth  
 937 Surface*, 118(3), 1342-1355.

- 938 Silva, T. A. M., Bigg, G. R., and Nicholls, K. W. (2006), Contribution of giant  
 939 icebergs to the Southern Ocean freshwater flux. *J. of Geophys. Res.: Oceans*,  
 940 111(C3).
- 941 Smith, K., B. Robison, J. Helly, R. Kaufmann, H. Ruhl, H., T. Shaw, and M. Vernet  
 942 (2007), Free-drifting icebergs: Hotspots of chemical and biological enrichment in  
 943 the Weddell Sea, *Science*, 317, 478482.
- 944 Shepherd, A., and D. Wingham (2007). Recent sea-level contributions of the Antarc-  
 945 tic and Greenland ice sheets. *Science*, 315(5818), 1529-1532.
- 946 Stern, A., D. M. Holland, P. R. Holland, A. Jenkins and J. Sommeria (2014), The  
 947 effect of geometry on ice shelf ocean cavity ventilation: a laboratory experiment.  
 948 *Experiments in Fluids*, 55(5), 1-19.
- 949 Stern, A., Johnson, E., Holland, D.M., Wagner, T.J., Wadhams, P., Bates, R.,  
 950 Abrahamsen, E.P., Nicholls, K.W., Crawford, A., Gagnon, J. and Tremblay, J.E.  
 951 (2015), Wind-driven upwelling around grounded tabular icebergs. *J. of Geophys.*  
 952 *Res.: Oceans*, 120(8), 5820-5835.
- 953 Stern, A., A. Adcroft, and O. Sergienko (2016), The effects of Antarctic iceberg  
 954 calving size distribution in a global climate model. *J. of Geophys. Res.: Oceans*,  
 955 121(8), 5773-5788.
- 956 Swope, W. C., H. C. Andersen, P. H. Berens, and K. R. Wilson (1982), A computer  
 957 simulation method for the calculation of equilibrium constants for the formation of  
 958 physical clusters of molecules: Application to small water clusters. *The Journal of*  
 959 *Chemical Physics* 76, no. 1, 637-649.
- 960 Tournadre, J., N. Bouvier, F. Girard-Ardhuin, and F. Remy (2016), Antarctic ice-  
 961 bergs distributions 1992-2014. *J. Geophys Res: Oceans*.
- 962 Turnbull I.D., N. Fournier, M. Stolwijk, T. Fosnaes, D. McGonigal (2015), Opera-  
 963 tional iceberg drift forecasting in Northwest Greenland, *Cold Reg. Sci. Technol.*  
 964 110, 1-18
- 965 Unger, J. D., 2014. Regulating the Arctic Gold Rush: Recommended Regulatory Re-  
 966 forms to Protect Alaska's Arctic Environment from Offshore Oil Drilling Pollution  
 967 . *Alaska L. Rev*, 31
- 968 Vernet, M., et al. (2012), Islands of ice: Influence of free-drifting Antarctic icebergs  
 969 on pelagic marine ecosystems, *Oceanography*, 25(3), 3839
- 970 Wagner, T. J. W., P. Wadhams, R. Bates, P. Elosegui, A. Stern, D. Vella, E. P.  
 971 Abrahamsen, A. Crawford, and K. W. Nicholls (2014), The footloose mechanism:  
 972 Iceberg decay from hydrostatic stresses. *Geophys. Res. Lett.*, 41(15), 5522-5529.
- 973 Weeks, W. F., and W. J. Campbell (1973). Icebergs as a fresh-water source: an  
 974 appraisal. *J. of Glaciol.*, 12(65), 207-233.
- 975 White, L., A. Adcroft, and R. Hallberg (2009), High-order regridding-remapping  
 976 schemes for continuous isopycnal and generalized coordinates in ocean models. *J.*  
 977 *of Comp. Phys.*, 228(23), 8665-8692.

Parameter	Symbol	Value	Unit
Domain Length	$L_x$	80	km
Domain Width	$L_y$	480	km
Horizontal Resolution	$\Delta x$	2	km
Number of vertical layers	$N_l$	72	non-dim
Horizontal Viscosity	$\nu_H$	6.0	$m^2 s^{-1}$
Diapycnal Viscosity	$\nu_V$	$10^{-3}$	$m^2 s^{-1}$
Horizontal Diffusivity	$\epsilon_H$	1.0	$m^2 s^{-1}$
Diapycnal Diffusivity	$\epsilon_V$	$5 \times 10^{-5}$	$m^2 s^{-1}$
Initial Surface Temperature	$T_t$	-1.9	$^{\circ}C$
Initial Bottom Temperature	$T_b$	1.0	$^{\circ}C$
Initial Surface Salinity	$S_t$	33.8	psu
Initial Bottom Salinity	$S_b$	34.7	psu
Maximum Ocean depth	$H_{ocean}$	720	m
Relaxation Time of Sponge Layer	$T_{sponge}$	0.1	days
Length of Sponge Layer	$L_{sponge}$	10	km
Ocean and iceberg model time step	$dt$	10	s
Elastic interactive force spring constant	$\kappa_e$	$10^{-5}$	$kg s^{-2}$

978 **Table 1.** Parameters used in the model. The ocean model parameters are as described in  
 979 Asay-Davis et al [2016]



980      **Figure 1.** Schematic showing how tabular icebergs are constructed using Lagrangian ele-  
 981      ments. (a) Hierarchy of ice elements' physical structure: (i) Previous icebergs models represent  
 982      icebergs using non-interacting point-particle elements; (ii) In the new framework ice elements are  
 983      given finite extent so that they are able to interact with the ocean across multiple grid cells, and  
 984      can interact with other elements; (iii) These finite extent elements can be joined together by nu-  
 985      merical bonds (magenta lines) to form larger structures such as tabular icebergs. (b) Areal pho-  
 986      tograph of a tabular iceberg with elements superimposed over it to illustrate how the Lagrangian  
 987      elements can be used to model tabular icebergs. In this schematic the ice elements (purple dots)  
 988      are initialized in a staggered lattice covering the surface area of the iceberg. For purposes of  
 989      mass aggregation, the ice elements are assumed to have hexagonal shape (red hexagons). For  
 990      purposes of element interactions, the ice elements are assumed to be circular (black circles).  
 991      Elements are initially bonded to adjacent elements using numerical bonds (magenta lines). These  
 992      numerical bonds form equilateral triangles which give the shape rigidity. An ocean grid has been  
 993      included (dashed cyan lines). The background photo is an areal photograph of iceberg PIIB  
 994      ( $\text{Area} = 42 \text{ km}^2$ ) taken in Baffin Bay in 2012. A red ship can be identified on the bottom of the  
 995      photo for scale.

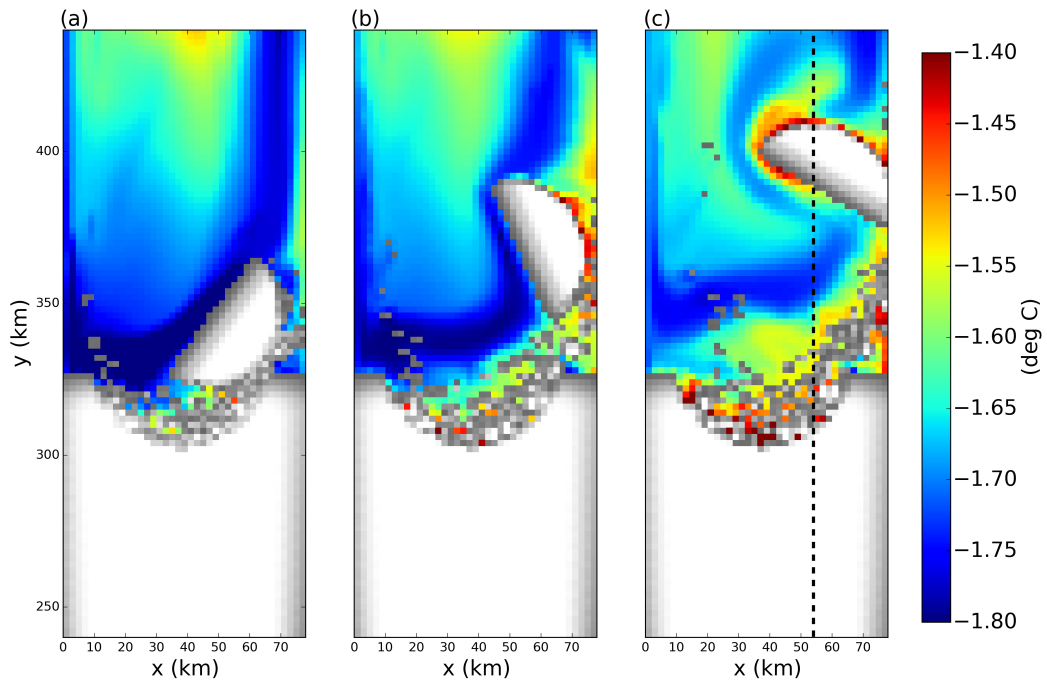
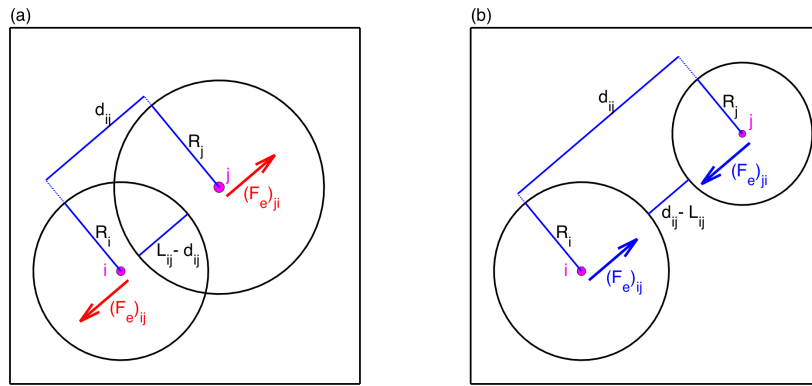
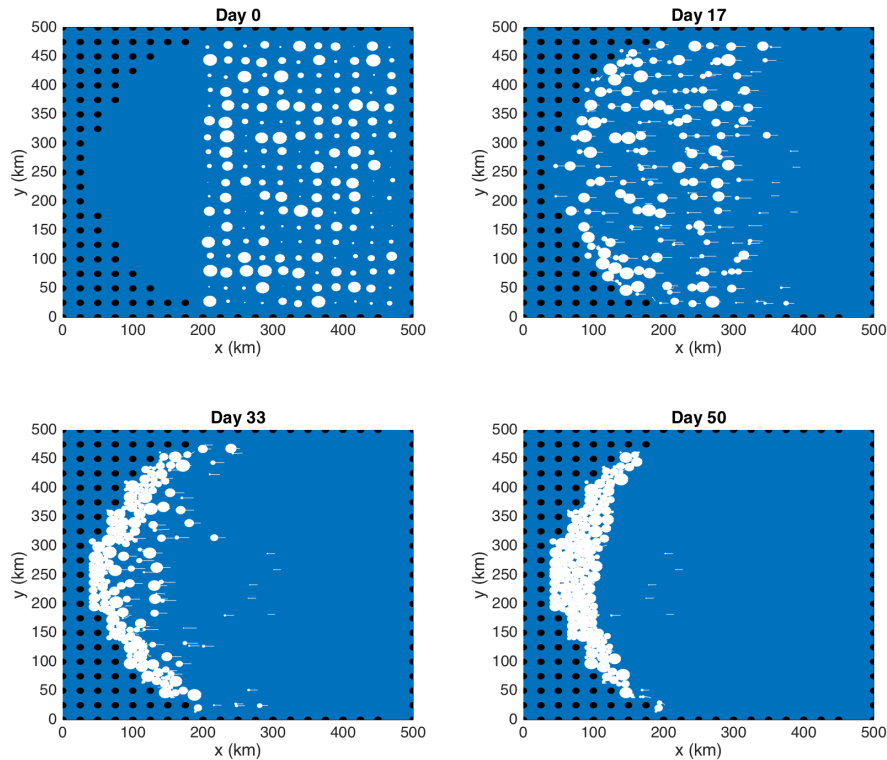


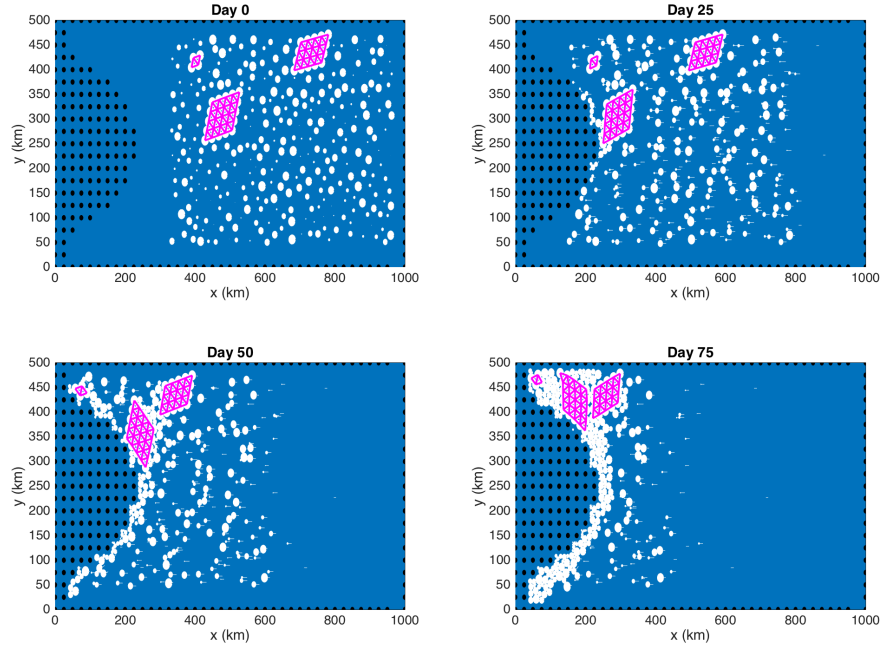
**Figure 2.** Snapshots of the sea surface temperature in the tabular iceberg calving simulation. Snapshots are taken (a) 7, (b) 15, and (c) 30 days after calving. Grid cells with ice mass  $> 10^4$  kg are plotted in white, with grey shading indicating thinner ice. The dashed line in panel (c) shows the location of the vertical transects shown in Figures 8 and 11.



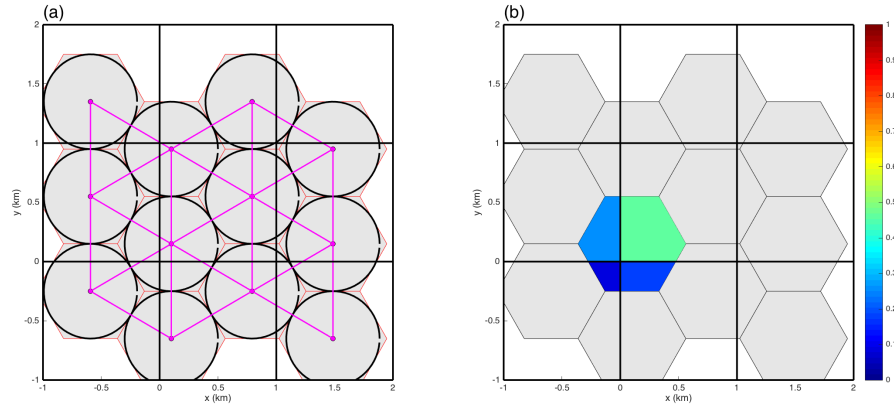
1000 **Figure 3.** Diagram showing the (a) repulsive and (b) attractive elastic interactive forces be-  
 1001 tween two elements,  $i$  and  $j$ .  $R_i$  and  $R_j$  are the interactive radii of element  $i$  and  $j$ , respectively.  
 1002  $d_{ij}$  is the distance between the centers of elements.  $L_{ij} = R_i + R_j$  is the critical-interaction-length  
 1003 scale.  $(F_e)_{ij}$  and  $(F_e)_{ji}$  are the elastic forces applied to elements  $i$  and  $j$ , respectively (equation  
 1004 7). A frictional damping force is also applied, which opposes the relative velocity of the elements  
 1005 (not shown). The attractive forces are only applied when the two elements are bonded together  
 1006 (i.e.:  $B_{ij} = 1$ ).



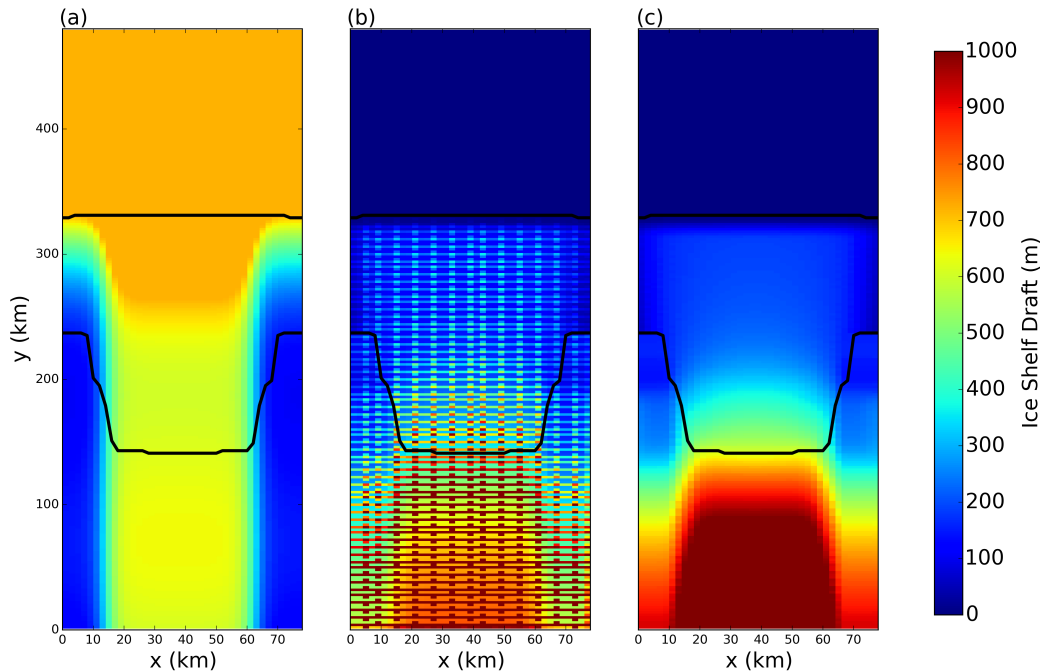
1007 **Figure 4.** Results of an uncoupled (ice-only) simulation with no bonds between ice elements.  
1008 Ice elements are initialized throughout the domain, as shown in the top left panel. The elements  
1009 are forced by an imposed westward ocean current of  $u=0.1\text{m/s}$  (no ocean model is used). Forces  
1010 due to sea surface slope, atmospheric drag, Coriolis and sea ice drag are set to zero. The figure  
1011 shows snapshots of ice element positions at time  $t=0, 17, 33$  and  $50$  days. The size of the dots  
1012 shows the surface area (and interaction radius) of each ice element. The white tails behind the  
1013 elements show the elements' positions over the preceding two days. Land points are shown by  
1014 black circles.



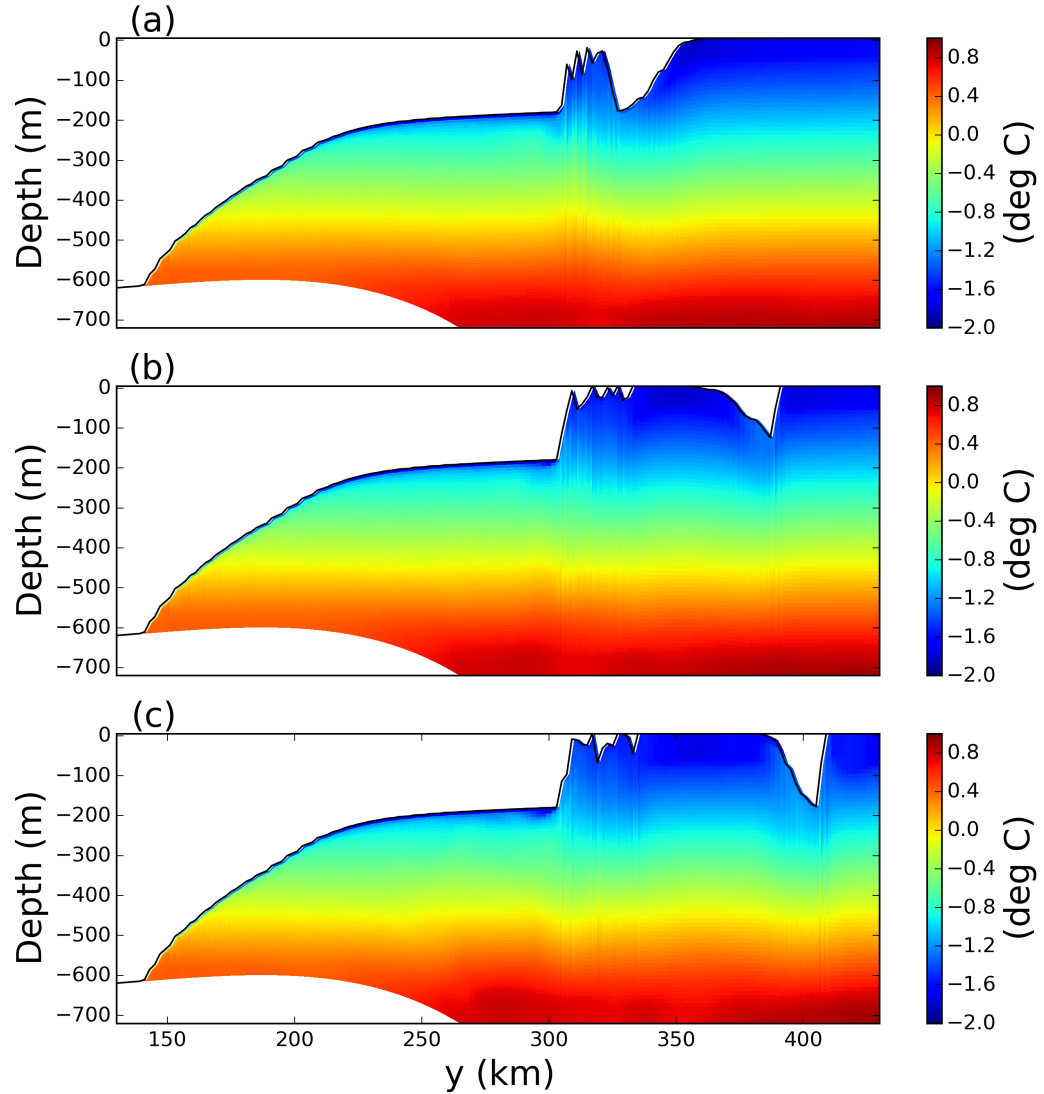
1015 **Figure 5.** Results of an uncoupled (ice-only) simulation using bonds between elements. Ice  
 1016 elements are initialized throughout the domain, as shown in the top left panel. Three tabular  
 1017 icebergs are included, with 25, 16 and 4 elements respectively. The elements are forced by an  
 1018 imposed westward ocean current of  $u=0.1\text{m/s}$  (no ocean model is used). Forces due to sea surface  
 1019 slope, atmospheric drag, Coriolis and sea ice drag are set to zero. The figure shows snapshots  
 1020 of ice element positions at time  $t=0, 25, 52$ , and  $75$  days. The size of the dots shows the sur-  
 1021 face area (and interaction radius) of each ice element. The white tails behind the elements show  
 1022 the elements' positions over the preceding two days. Bonds between ice elements are plotted in  
 1023 magenta. Land points are shown by black circles.



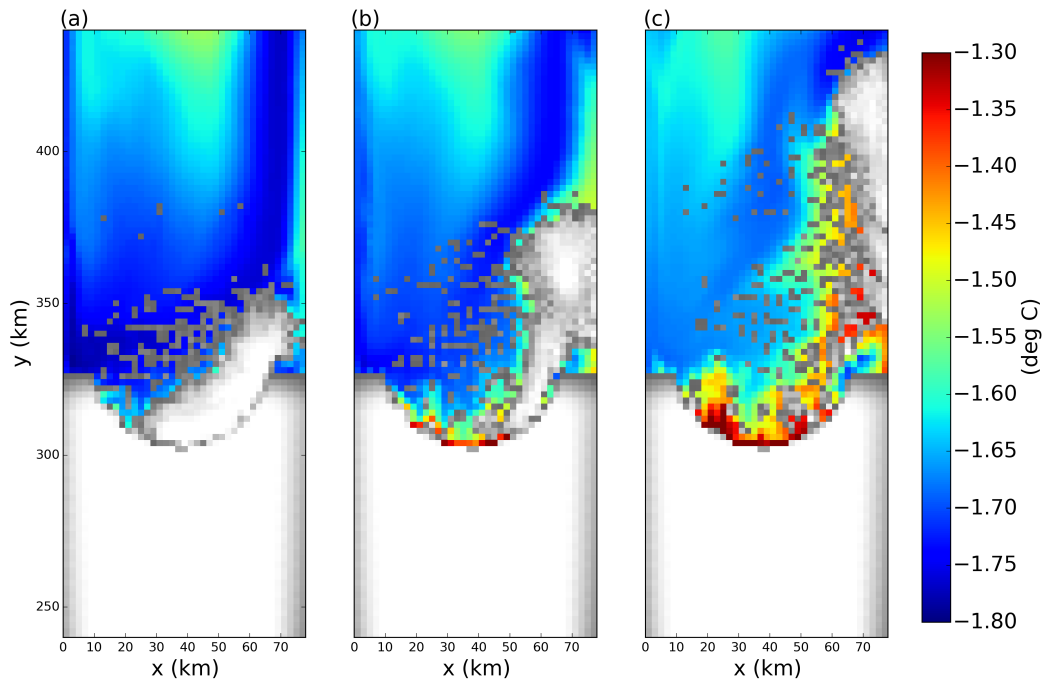
1024      **Figure 6.** (a) Ice element packing and geometry: ice elements (purple dots) are initialized  
 1025      in a staggered lattice. For purposes of mass aggregation, the ice elements are assumed to have  
 1026      hexagonal shape (red hexagons). For purposes of element interactions, the ice elements are  
 1027      assumed to be circular (black circles). Elements are initially bonded to adjacent elements us-  
 1028      ing numerical bonds (magenta lines). (b) Intersection of an hexagonal element and the ocean  
 1029      grid. The colors indicate the fraction of the hexagon that lies in each grid cell. These fractions  
 1030      are used as weights to spread the iceberg model properties to the ocean grid (see text for more  
 1031      details).



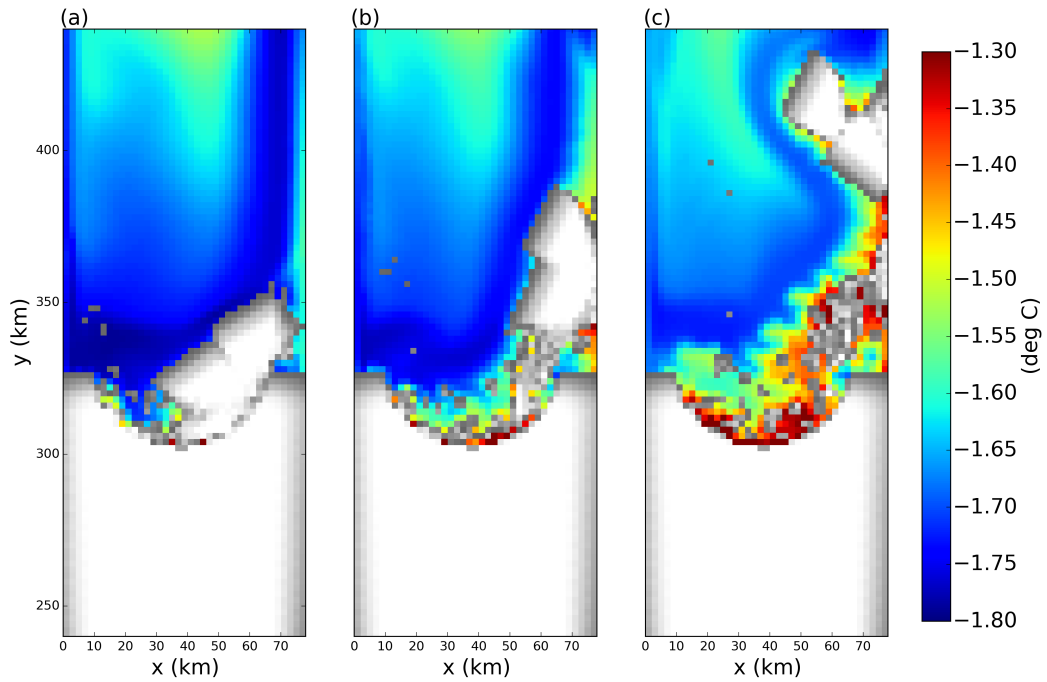
1032      **Figure 7.** (a) Ocean bottom topography and (c) ice-shelf draft used to initialized the tabular  
1033      iceberg calving simulation. The ice draft is calculated from the total mass in an ocean grid cell  
1034      after the mass-spreading interpolation has been applied (as explained in Section 2.3). Panel (b)  
1035      shows the initial ice draft that would be calculated if the mass-spreading interpolation were not  
1036      used (i.e. elements treated as point masses).



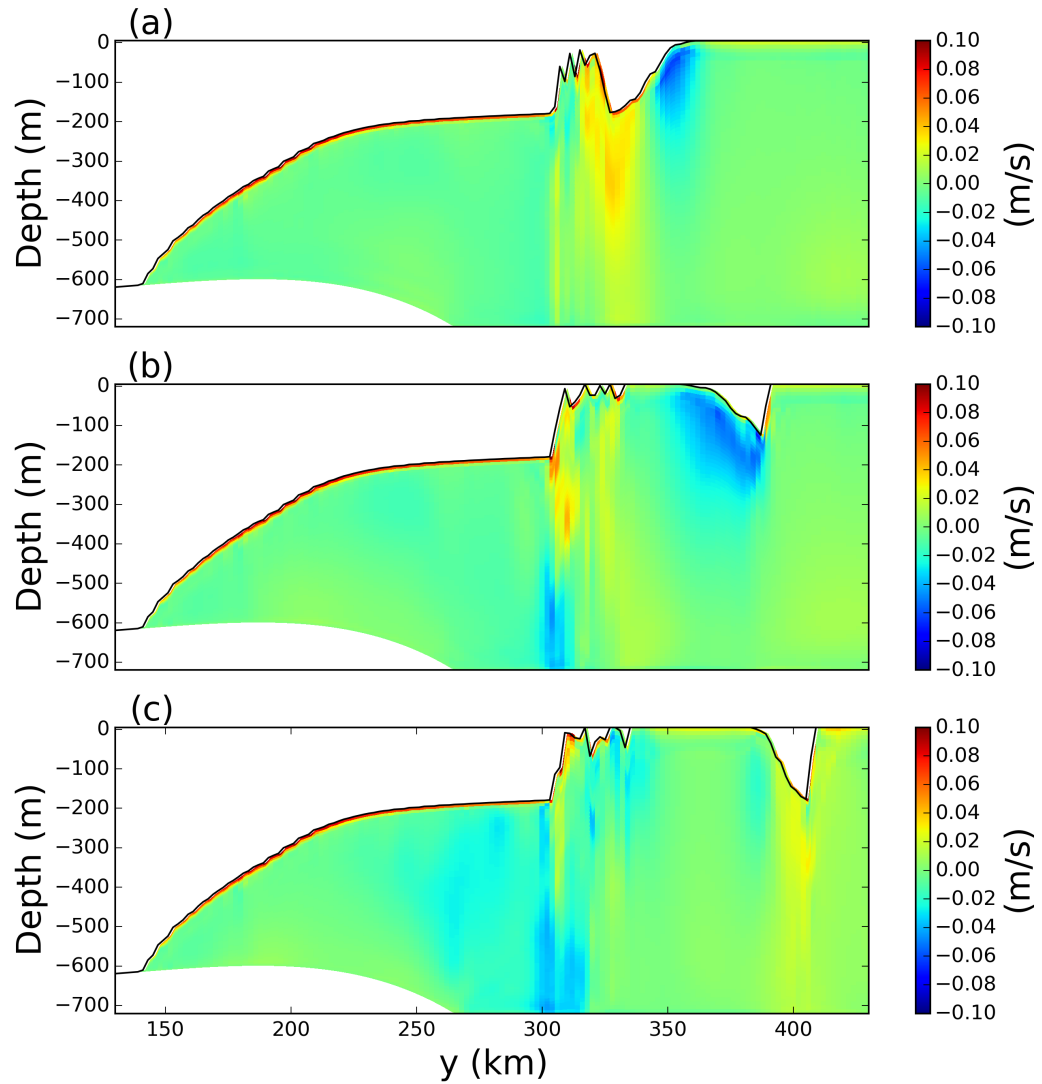
1037 **Figure 8.** Snapshots of vertical sections of ocean temperature at  $x = 54$  km in the tabular-  
1038 iceberg-calving Control experiment. Snapshots are taken (a) 7, (b) 15, and (c) 30 days after  
1039 calving. The position of the vertical transects is shown by the dashed lines in Figure 2c.



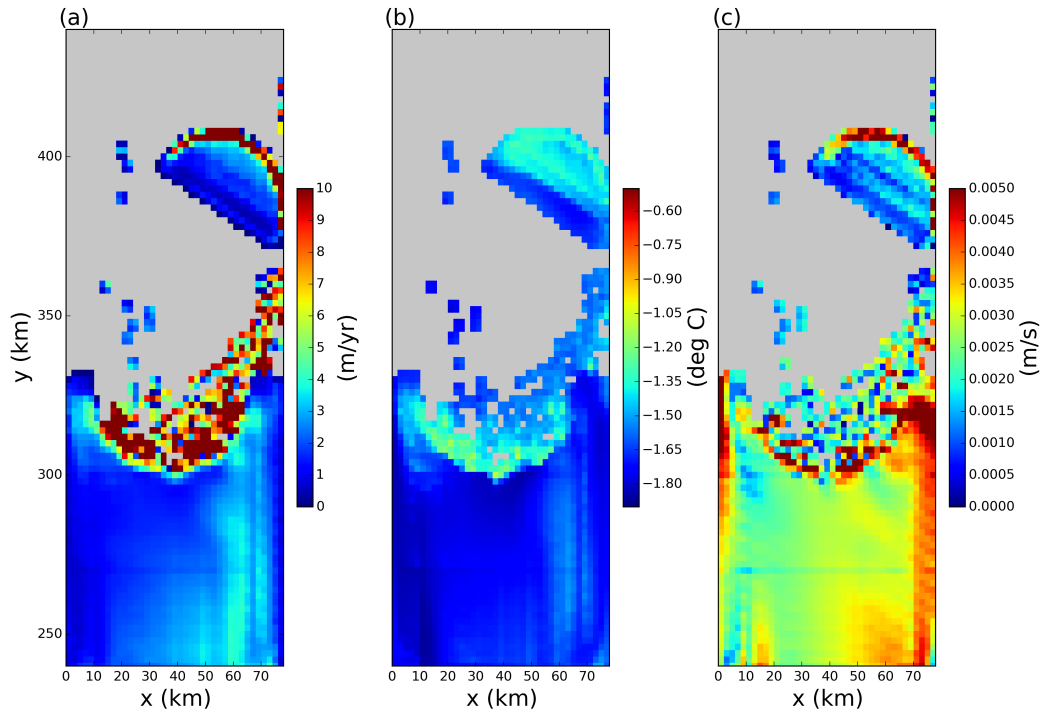
1040      **Figure 9.** No bonds simulation: Snapshots of the sea surface temperature for a simulation  
1041      where all bonds have been broken. Snapshots are taken (a) 7, (b) 15, and (c) 30 days after calv-  
1042      ing. Grid cells with ice mass  $\gtrsim 10^4$  kg are plotted in white, with grey shading indicating thinner  
1043      ice.



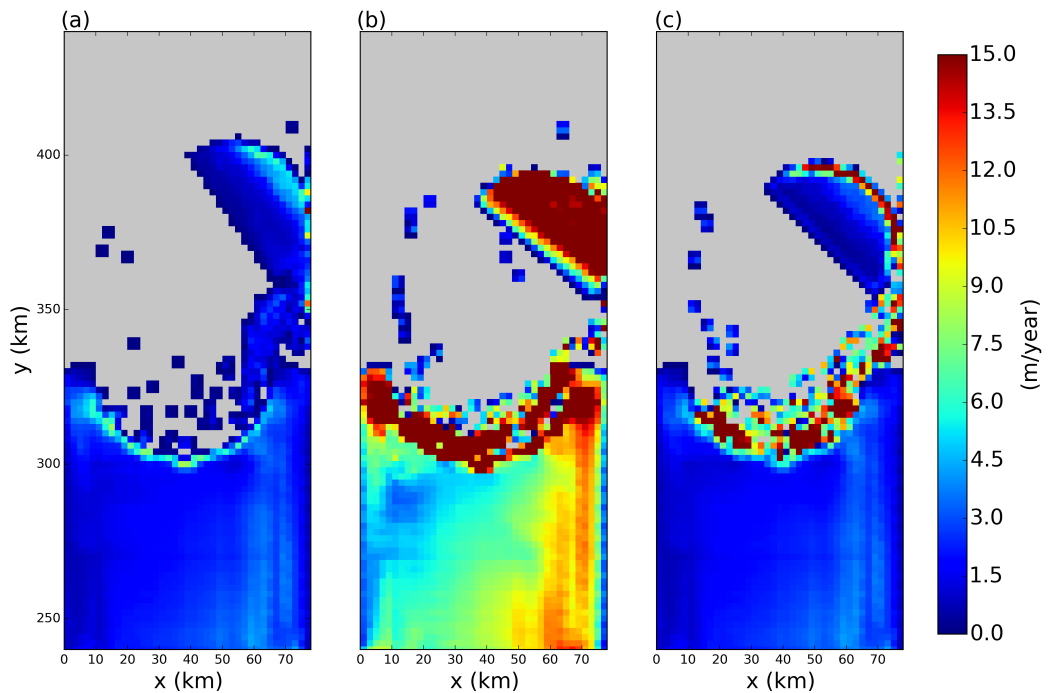
1044 **Figure 10.** Iceberg splitting simulation: Snapshots of the sea surface temperature for the ice-  
1045 berg splitting simulation. Snapshots are taken (a) 7, (b) 15, and (c) 30 days after calving. Grid  
1046 cells with ice mass  $\geq 10^4$  kg are plotted in white, with grey shading indicating thinner ice.



1047      **Figure 11.** Snapshots of vertical sections of meridional velocity at  $x=54$  km in the tabular-  
1048      iceberg-calving Control experiment. Snapshots are taken (a) 7, (b) 15, and (c) 30 days after  
1049      calving. The position of the transects is shown by the dashed line in Figure 2c.



1050      **Figure 12.** Results of the tabular-iceberg-calving experiment 30 days after the iceberg calves.  
1051      The three panels show snapshots of the (a) melt rate, (b) top-of-ocean temperature and (c) the  
1052      frictional velocity,  $u^*$ , at the base of the ice shelf. Ocean grid cells without ice are masked out in  
1053      grey.



1054      **Figure 13.** Results of the tabular-iceberg-calving experiment using three different melt-rate  
 1055      parametrization. Panels show snapshots of the melt rate 30 days after calving for simulations us-  
 1056      ing the (a) three-equation melt-rate parametrization, (b) icebergs-drift melt-rate parametrization,  
 1057      (c) mixed-melt-rate parametrization (as described in Section 2.5.). Ocean grid cells without ice  
 1058      are masked out in grey.